

# Probing Two Dark Dimensions through Primordial Black Holes, Gravitational Waves, and Colliders

Waqas Ahmed<sup>1a</sup>, George K. Leontaris<sup>2b</sup>

<sup>1</sup> *Center for Fundamental Physics, School of Artificial Intelligence, Hubei Polytechnic University, Huangshi 435003, China.*

<sup>2</sup> *Physics Department, University of Ioannina, 45110, Ioannina, Greece.*

We study primordial-black-hole (PBH) dark matter in the two-dark-dimensions (2DD) framework, a six-dimensional brane-world scenario with two compact extra dimensions and a fundamental gravity scale of order 10 TeV. We calculate the evolution of higher-dimensional PBHs including the recently proposed quantum-gravitational memory-burden effect. For a memory exponent  $p = 2$ , the evaporation rate is strongly suppressed, allowing PBHs with initial masses as small as  $\sim 10^{-3}$  g to survive until the present epoch. Consequently, PBHs can account for the observed dark matter over a mass range extending from  $10^{-3}$  g to  $10^{21}$  g. We further compute the stochastic gravitational-wave background generated at second order by the primordial curvature perturbations responsible for PBH formation. We show that the conventional four-dimensional formalism for scalar-induced gravitational waves remains applicable throughout the mass range accessible to current and future gravitational wave experiments. The resulting signals can be probed by LISA, DECIGO, and pulsar timing arrays. Using Fisher forecasts, we find that these observations can constrain the PBH mass, dark-matter fraction, and width of the primordial curvature spectrum with high precision. The low fundamental gravity scale of the 2DD framework also permits the production of microscopic black holes at future high-energy colliders. Their decay signatures, together with gravitational-wave measurements, provide complementary tests of higher-dimensional gravity, the memory-burden mechanism, and primordial-black-hole dark matter.

## I. INTRODUCTION

The large hierarchy between the electroweak scale,  $M_{\text{EW}} \sim 100$  GeV, and the four-dimensional Planck scale,  $M_{\text{Pl}} \sim 10^{18}$  GeV, remains one of the central puzzles in fundamental physics. A well-known way to address this problem is provided by large-extra-dimensional scenarios [1–3], in which the Standard Model (SM) fields are localized on a three-brane while gravity propagates in a higher-dimensional bulk. If the compact space has volume  $\mathcal{V}_n$ , the fundamental quantum-gravity scale  $M_*$  is related to the four-dimensional Planck scale by

$$M_{\text{Pl}}^2 = M_*^{2+n} \mathcal{V}_n. \quad (1)$$

For sufficiently large compact dimensions,  $M_*$  can be lowered to the multi-TeV range, thereby softening the electroweak hierarchy problem.

At the same time, the Swampland programme [4, 5] (see also reviews [6–9]) provides a framework for identifying low-energy effective field theories that may consistently couple to quantum gravity. One of its striking implications is the Dark Dimension proposal [10], in which the observed smallness of the cosmological constant is related to the existence of a large compact dimension. The corresponding Kaluza–Klein (KK) scale is naturally very light, which can have potentially important consequences for cosmology, neutrino physics, and primordial black holes (PBHs) [11–13].

Recently, this idea was extended to the case of two compact dark dimensions,  $\mathbf{n} = 2$  [14, 15].<sup>1</sup> In this six-dimensional (6d) two-dark-dimensions framework, the fundamental gravity scale is reduced to

$$M_* \sim 10 \text{ TeV}, \quad (2)$$

making the scenario potentially testable at future high-energy colliders such as the Future Circular Collider (FCC) [16–18]. For a square two-torus with compactification length  $L = 2\pi R$ , the reduced Planck mass satisfies

$$M_{\text{Pl}}^2 = M_*^4 L^2, \quad (3)$$

and the characteristic KK mass gap is

$$\Delta m_{\text{KK}} \simeq \frac{1}{L} = \frac{M_*^2}{M_{\text{Pl}}} \simeq 3.1 \times 10^{-2} \text{ eV} \left( \frac{M_*}{8.7 \text{ TeV}} \right)^2. \quad (4)$$

<sup>a</sup> E-mail: [waqasmit@hbpu.edu.cn](mailto:waqasmit@hbpu.edu.cn)

<sup>b</sup> E-mail: [leonta@uoi.gr](mailto:leonta@uoi.gr)

<sup>1</sup> For a recent review, see Ref. [9].

Equivalently, for  $M_* \simeq 10$  TeV the gap is of order  $4 \times 10^{-2}$  eV, close to the atmospheric neutrino mass scale [19]. Thus the two-dark-dimensions scenario links the hierarchy problem, the dark-energy scale, and neutrino physics while remaining phenomenologically testable.

Primordial black holes, formed through the gravitational collapse of large primordial curvature perturbations [20, 21], have long been studied as possible dark-matter candidates. In standard four-dimensional cosmology, PBHs lighter than approximately  $5 \times 10^{14}$  g evaporate before the present epoch, while heavier PBHs are strongly constrained by microlensing, gamma-ray observations, and cosmic microwave background energy-injection bounds [22]. However, in higher-dimensional theories, the evaporation law is modified. In the five dark dimensions, rotating PBHs may survive to masses as low as  $M \sim 10^{10}$  g [12]. In six dimensions the effect is even more striking. As shown in Ref. [15] the 6d PBHs evaporate more slowly, and when the quantum-gravitational memory-burden effect [23, 24] is included with exponent  $p = 2$ , the lifetime is enhanced enough to allow PBHs as light as

$$M_{\text{PBH}} \sim 10^{-3} \text{ g}, \quad (5)$$

to survive until today. This opens a broad dark-matter window,

$$10^{-3} \text{ g} \lesssim M_{\text{PBH}} \lesssim 10^{21} \text{ g}, \quad (6)$$

subject to the usual cosmological and astrophysical constraints.

The same primordial curvature perturbations responsible for PBH formation inevitably generate a stochastic background of gravitational waves at second order in cosmological perturbation theory [25, 26]. These scalar-induced gravitational waves (SIGWs) have been extensively studied in the four-dimensional setting [27, 28] and provide an independent probe of the PBH formation mechanism. In the present six dimensional scenario, however, one must distinguish carefully between two regimes. The relevant comparison is between two fundamental scales:

1. The physical momentum of the scalar mode at horizon re-entry, which is equivalent to the Hubble scale at PBH formation,

$$H_{\text{form}} \simeq \frac{4\pi\gamma M_{\text{Pl}}^2}{M_{\text{PBH}}}, \quad \gamma \simeq 0.2, \quad (7)$$

where  $M_{\text{PBH}}$  is the PBH mass and  $\gamma$  is the efficiency factor for gravitational collapse.

2. The KK mass gap, set by the compactification radius  $R$  of the extra dimensions:

$$m_{\text{KK}} \equiv \frac{1}{2\pi R}. \quad (8)$$

This threshold determines whether KK modes can be excited. The boundary between the two regimes occurs when these scales coincide,  $H_{\text{form}} = m_{\text{KK}}$ . Solving for the corresponding PBH mass defines the critical mass:

$$M_{\text{KK}} \equiv \frac{\gamma M_{\text{Pl}}^2}{2m_{\text{KK}}} \simeq 8.5 \times 10^{23} \text{ g}. \quad (9)$$

This yields the following physical picture:

- **Regime I:**  $M_{\text{PBH}} \gtrsim M_{\text{KK}}$  (heavy PBHs). In this case  $H_{\text{form}} \lesssim m_{\text{KK}}$ , massive KK gravitons are not kinematically excited, the extra dimensions are not probed, and the usual four-dimensional SIGW formalism is a rigorous effective description.
- **Regime II:**  $M_{\text{PBH}} \lesssim M_{\text{KK}}$  (light PBHs). In this case  $H_{\text{form}} \gtrsim m_{\text{KK}}$ , the KK tower can be excited, and a complete treatment requires the full six-dimensional tensor dynamics. The standard four-dimensional SIGW result should then be interpreted as a zero-mode benchmark or exploratory estimate rather than a complete prediction.

Since the full PBH dark-matter window considered in this work,  $10^{-3} \text{ g} \lesssim M_{\text{PBH}} \lesssim 10^{21} \text{ g}$ , lies below  $M_{\text{KK}}$ , the SIGW signals associated with this window belong to Regime II. Accordingly, throughout this paper we use the standard four-dimensional SIGW spectrum as a benchmark for the massless zero-mode contribution, while emphasizing that the full six-dimensional KK contribution is model-dependent and requires a dedicated calculation.

The low fundamental scale  $M_* \sim 10$  TeV also allows microscopic black holes to be produced at future colliders if the partonic centre-of-mass energy exceeds the fundamental gravity scale [29, 30]. Such black holes would decay through Hawking radiation into high-multiplicity final states [30–33], with possible missing energy carried by bulk

gravitational modes. Their mass temperature relation, event multiplicity, and missing-energy pattern would provide complementary probes of the number of extra dimensions and of the fundamental scale of gravity.

In this work we study PBH dark matter, scalar-induced gravitational waves, and collider signatures in the 6d two-dark-dimensions scenario. We first review the evaporation of six-dimensional PBHs, including the memory-burden effect [23, 24, 34, 35], and identify the broad dark-matter window  $10^{-3} \text{ g} \lesssim M_{\text{PBH}} \lesssim 10^{21} \text{ g}$  for  $p = 2$ . We then compute the associated zero-mode benchmark SIGW spectra for a log-normal primordial curvature power spectrum, following the standard scalar-induced gravitational-wave formalism [25, 26, 28, 36, 37], and discuss the validity of the four-dimensional approximation in terms of the Regime I and Regime II classification above. We also perform Fisher forecasts for future gravitational-wave observatories [38–43], treating the benchmark spectrum as a phenomenological probe of the PBH mass, abundance, and spectral width. Finally, we discuss the collider phenomenology of six-dimensional microscopic black holes, including their production cross section, Hawking temperature, multiplicity, and possible missing-energy signatures [31–33, 44–47].

The paper is organised as follows. Section II introduces the two-dark-dimensions framework and the evaporation of six-dimensional PBHs. Section III discusses the memory-burden effect, near-extremal extensions, and the resulting dark-matter window. Section IV presents the scalar-induced gravitational-wave calculation and the Regime I/Regime II validity analysis. The Fisher forecast methodology and projected constraints are presented next. Section VI discusses collider signatures of microscopic six-dimensional black holes, mono-jet events, and virtual graviton exchange. We conclude in Sec. VII.

## II. THE TWO-DARK-DIMENSIONS SCENARIO

We consider a six-dimensional spacetime of the form  $\mathcal{M}_4 \times T^2$ , where the two additional spatial dimensions are flat and compact. Gravity propagates in the full six-dimensional bulk, while the Standard Model fields are localized on a four-dimensional brane [1–3]. The six-dimensional gravitational dynamics are governed by

$$S_6 = \frac{M_*^4}{2} \int d^4x d^2y \sqrt{-G} \mathcal{R}(G), \quad (10)$$

where  $M_*$  is the reduced six-dimensional Planck scale and  $\mathcal{R}(G)$  is the Ricci scalar constructed from the six-dimensional metric  $G_{MN}$ . After compactification, the four-dimensional reduced Planck mass is related to the fundamental scale through the volume of the compact space,

$$M_{\text{Pl}}^2 = M_*^4 V_2, \quad (11)$$

where  $V_2$  refers to the ‘volume’ of the two extra dimensions and for a square two-torus with geometric radius  $R$  and periods  $2\pi R$ , one has

$$V_2 = (2\pi R)^2, \quad M_{\text{Pl}}^2 = M_*^4 (2\pi R)^2. \quad (12)$$

With the benchmark value  $R \simeq 1 \mu\text{m}$ , this gives

$$M_* = \left( \frac{M_{\text{Pl}}^2}{(2\pi R)^2} \right)^{1/4} \simeq 8.7 \times 10^3 \text{ GeV} \sim 10 \text{ TeV}. \quad (13)$$

Thus, the fundamental gravity scale lies close to the energy range targeted by future high-energy colliders [17, 18].

Compactification gives rise to a tower of Kaluza–Klein excitations [48–50]. For a two-torus with periods  $2\pi R$ , the wavefunctions read  $\exp(in_i y_i / R)$  and the KK mass spectrum is

$$m_{\vec{n}} = \frac{\sqrt{n_1^2 + n_2^2}}{R}, \quad \vec{n} = (n_1, n_2) \in \mathbb{Z}^2. \quad (14)$$

The lightest non-zero KK mass – *i.e.* the physical mass gap of the tower – is therefore

$$\Delta m_{\text{KK}} \equiv m_{(1,0)} - m_{(0,0)} = \frac{1}{R} = 2\pi \frac{M_*^2}{M_{\text{Pl}}} \simeq 1.97 \times 10^{-1} \text{ eV} \left( \frac{1 \mu\text{m}}{R} \right). \quad (15)$$

It is sometimes convenient to introduce the reduced length

$$L \equiv 2\pi R, \quad (16)$$

so that the Planck/string relation becomes

$$\frac{1}{L} = \frac{M_*^2}{M_{\text{Pl}}} \simeq 3.1 \times 10^{-2} \text{ eV} \left( \frac{M_*}{8.7 \text{ TeV}} \right)^2. \quad (17)$$

Note that  $1/L$  is *not* the physical KK mass gap; it is related to it by

$$\Delta m_{\text{KK}} = \frac{1}{R} = \frac{2\pi}{L}. \quad (18)$$

In what follows we adopt the strict geometric torus convention, *i.e.* we always take  $\Delta m_{\text{KK}} = 1/R$  as the physical gap.

The presence of extra dimensions modifies the properties of black holes formed in the early Universe. For black holes whose horizon radius is smaller than the compactification scale, the appropriate non-rotating solution is the six-dimensional Schwarzschild–Tangherlini geometry [51, 52]. With normalization in Eq. (10), the horizon radius satisfies

$$r_h^3 = \frac{3M_{\text{BH}}}{16\pi^2 M_*^4}, \quad (19)$$

or equivalently

$$r_h = k_6 \frac{1}{M_*} \left( \frac{M_{\text{BH}}}{M_*} \right)^{1/3}, \quad k_6 = \left( \frac{3}{16\pi^2} \right)^{1/3}. \quad (20)$$

Up to the numerical coefficient  $k_6$ , this gives the scaling  $r_h \propto M_{\text{BH}}^{1/3}$ . The Hawking temperature is [53],

$$T_{\text{BH}} = \frac{d-3}{4\pi r_h} = \frac{3}{4\pi r_h} \propto M_{\text{BH}}^{-1/3}, \quad (21)$$

and the Bekenstein–Hawking entropy scales as [54],

$$S_{\text{BH}} = \frac{A_4}{4G_6} \propto M_*^4 r_h^4 \propto \left( \frac{M_{\text{BH}}}{M_*} \right)^{4/3}, \quad (22)$$

where  $A_4$  is the horizon 4-area and  $G_6 = (8\pi M_*^4)^{-1}$ . The six-dimensional Hawking luminosity is set by the Stefan–Boltzmann scaling law for  $d = 6$ :

$$-\frac{dM}{dt} = \frac{C_M}{r_h^2}, \quad (23)$$

where  $C_M$  is a dimensionless coefficient which encodes the greybody factors and the number of available particle species [33, 47, 55]. Integrating the above, gives the lifetime

$$\tau_0(M) \propto \int^M dM' r_h^2(M') \propto M^{5/3} M_*^{-8/3}. \quad (24)$$

A convenient phenomenological normalization is

$$\tau_0(M) \simeq 13.7 \left( \frac{M}{10^8 \text{ g}} \right)^{5/3} \left( \frac{10 \text{ TeV}}{M_*} \right)^{8/3} \left( \frac{C_{M,0}}{C_M} \right) \text{ Gyr}, \quad (25)$$

where  $C_{M,0}$  denotes the reference greybody coefficient used to obtain the quoted numerical normalization. Thus, in the conventional six-dimensional Hawking picture, PBHs with masses of order  $M \gtrsim 10^8 \text{ g}$  survive until the present epoch, while lighter PBHs require an additional lifetime-enhancing mechanism. If the PBH is initially rotating, its early evolution is described by the six-dimensional Myers–Perry solution [56] with a single spin parameter. The horizon radius is related to the non-rotating (Schwarzschild) radius  $r_s$  ( see Eq. (20)) by

$$r_h = \frac{r_s}{(1+a_*^2)^{1/3}}, \quad r_s = k_6 \frac{1}{M_*} \left( \frac{M_{\text{BH}}}{M_*} \right)^{1/3}, \quad (26)$$

where  $a_* = a/r_h$  is the dimensionless spin parameter. The corresponding Hawking temperature for  $n = 2$  extra dimensions is

$$T_{\text{MP}} = \frac{3 + a_*^2}{4\pi r_h(1 + a_*^2)}. \quad (27)$$

For  $a_* \rightarrow 0$  one recovers the Schwarzschild result  $T_{\text{MP}} = 3/(4\pi r_s)$ , as required.

Rotation modifies the evaporation through coupled mass and angular momentum loss rates,

$$\frac{dM}{dt} = -\frac{C_M(a_*)}{r_h^2}, \quad \frac{dJ}{dt} = -\frac{C_J(a_*)}{r_h}, \quad (28)$$

where  $C_M(a_*)$  and  $C_J(a_*)$  encode spin-dependent greybody factors and the particle spectrum [47, 57–59]. During the spin-down stage the black hole loses angular momentum efficiently and subsequently approaches a Schwarzschild–Tangherlini configuration. The later evolution can then be treated using the non-rotating scaling laws above. If the memory-burden effect becomes important at late times, the evaporation history separates into three stages: an initial spin-down phase, an approximately Schwarzschild-like Hawking phase, and a final memory-burdened phase in which the emission rate is suppressed.

### III. MEMORY BURDEN, NEAR-EXTREMALITY, AND THE DARK-MATTER WINDOW

The evaporation history of a six-dimensional primordial black hole (PBH) depends on whether the black hole is non-rotating, rotating, or near-extremal. In this section we clarify these regimes and derive the corresponding lifetime scalings. This distinction is important because ordinary non-extremal PBHs and near-extremal charged PBHs have different temperature suppressions and therefore different mass dependences.

#### A. Ordinary six-dimensional evaporation

We first recall the ordinary non-extremal evaporation regime. For a six-dimensional Schwarzschild–Tangherlini PBH with horizon radius below the compactification scale, the horizon radius is given by Eq. (20). The corresponding entropy scales as Eq. (22), namely  $S_{\text{BH}} \propto (M_{\text{BH}}/M_*)^{4/3}$ .

The standard semiclassical mass-loss rate is given by Eq. (23). Since the horizon radius scales as  $r_h \propto M_{\text{BH}}^{1/3}$ , the evaporation time follows the six-dimensional scaling derived in Eq. (24),

$$\tau_0(M_{\text{BH}}) \propto M_{\text{BH}}^{5/3} M_*^{-8/3}.$$

Using the numerical normalization in Eq. (25), ordinary six-dimensional PBHs survive until the present epoch only for masses of order

$$M_{\text{BH}} \gtrsim 10^8 \text{ g},$$

up to the uncertainty associated with the greybody coefficient and the available particle spectrum. Lighter PBHs would have evaporated completely and therefore cannot constitute a viable dark matter candidate unless their lifetime is extended beyond the standard Hawking estimate. This could be achieved, for instance, by the memory-burden effect [23, 24] or by near-extremal temperature suppression, both of which would allow the mass range to be extended downward.

If the PBH is initially rotating, the early evolution is instead described by the six-dimensional Myers–Perry solution. The relation between the rotating horizon radius and the non-rotating radius was given in Eq. (26), while the spin-dependent temperature and the coupled mass/angular-momentum loss equations were given in Eqs. (27) and (28). The spin-down stage is typically efficient, so the PBH subsequently approaches a nearly Schwarzschild–Tangherlini configuration. Consequently, the late-time ordinary evaporation of an initially rotating PBH is controlled by the same six-dimensional scaling,

$$\tau_0(M_{\text{BH}}) \propto M_{\text{BH}}^{5/3},$$

with only spin-dependent numerical corrections inherited from the early spin-down phase.

## B. Memory-burdened evaporation

The memory-burden mechanism modifies the late-time evaporation law of a black hole. The basic idea is that Hawking emission does not only reduce the black-hole mass, but also changes the state of a large number of internal memory modes. Once the number of emitted Hawking quanta becomes comparable to the Bekenstein–Hawking entropy, these modes can backreact on the evaporation process and suppress further emission.

This effect is parametrized phenomenologically by multiplying the standard Hawking rate by an entropy-suppression factor,

$$-\dot{M}_{\text{BH}}^{\text{MB}} \equiv -\left. \frac{dM_{\text{BH}}}{dt} \right|_{\text{MB}} = \frac{1}{S_{\text{BH}}^p} \left( -\frac{dM_{\text{BH}}}{dt} \right)_{\text{std}}, \quad (29)$$

where  $p > 0$  is a model-dependent memory-burden exponent. For an ordinary non-extremal PBH after the spin-down stage, the geometry is well approximated by the six-dimensional Schwarzschild–Tangherlini solution. Using Eqs. (23) and (22), one therefore obtains

$$-\dot{M}_{\text{BH}}^{\text{MB}} = \frac{C_M^{(0)}}{r_s^2 S_{\text{BH}}^p}, \quad (30)$$

where  $r_s$  is the non-rotating six-dimensional horizon radius and  $C_M^{(0)}$  denotes the corresponding greybody coefficient. In this phenomenological treatment, the greybody coefficient is assumed to be unchanged by the memory burden; the suppression is encoded entirely in the factor  $S_{\text{BH}}^{-p}$ .

A useful way to motivate the onset of the memory-burdened phase is to introduce a critical occupation number  $N_c \simeq S_{\text{BH}}$ . In a schematic microscopic description, the energy gap of the memory modes may be written as

$$E_K(n_0) = \left( 1 - \frac{n_0}{N_c} \right)^p \epsilon_K, \quad N_c \simeq S_{\text{BH}}, \quad \epsilon_K \simeq \sqrt{S_{\text{BH}}} r_s^{-1}. \quad (31)$$

The memory modes correspond to soft excitations that store information about the black hole’s quantum state. The occupation number  $n_0$  counts how many Hawking quanta have been emitted. At early times  $n_0 \ll N_c$ , so the memory modes are energetically costly to excite and the black hole evaporates approximately at the standard Hawking rate. As evaporation proceeds,  $n_0$  increases and the gap decreases. When  $n_0$  becomes comparable to  $N_c$ , the memory modes become nearly degenerate and the evaporation rate is suppressed.

The onset of the memory-burdened phase may be characterized by the fractional mass loss

$$q \equiv \frac{\Delta M_{\text{crit}}}{M_0} \sim [p S_{\text{BH}}(M_0)]^{-1/p}, \quad (32)$$

where  $M_0$  is the initial PBH mass. Thus,

$$p = 1 : \quad q \sim S_{\text{BH}}^{-1}, \quad p = 2 : \quad q \sim (2S_{\text{BH}})^{-1/2}. \quad (33)$$

Since macroscopic PBHs have  $S_{\text{BH}} \gg 1$ , the memory-burdened phase can begin after only a small fractional mass loss. The subsequent lifetime, however, depends sensitively on the exponent  $p$ .

Using Eq. (30), the memory-burdened lifetime scales as

$$\tau_{\text{MB}}^{(p)}(M_{\text{BH}}) \sim \int^{M_{\text{BH}}} dM' r_s^2(M') S_{\text{BH}}^p(M'). \quad (34)$$

The required mass dependences are already given in Eqs. (20) and (22):

$$r_s^2 \propto M_{\text{BH}}^{2/3} M_*^{-8/3}, \quad S_{\text{BH}}^p \propto \left( \frac{M_{\text{BH}}}{M_*} \right)^{4p/3}.$$

Therefore,

$$\begin{aligned} \tau_{\text{MB}}^{(p)}(M_{\text{BH}}) &\propto \int^{M_{\text{BH}}} dM' (M')^{2/3} M_*^{-8/3} \left[ (M')^{4/3} M_*^{-4/3} \right]^p \\ &\propto \frac{1}{M_*} \left( \frac{M_{\text{BH}}}{M_*} \right)^{(4p+5)/3}. \end{aligned} \quad (35)$$

Equivalently, at fixed  $M_*$ ,

$$\tau_{\text{MB}}^{(p)}(M_{\text{BH}}) \propto M_{\text{BH}}^{(4p+5)/3}. \quad (36)$$

The important special cases are

$$p = 0: \quad \tau \propto M_{\text{BH}}^{5/3}, \quad p = 1: \quad \tau \propto M_{\text{BH}}^3, \quad p = 2: \quad \tau \propto M_{\text{BH}}^{13/3}. \quad (37)$$

The case  $p = 0$  reproduces the standard six-dimensional Hawking result, while  $p = 1$  and  $p = 2$  correspond to increasingly strong entropy suppression and therefore to substantially longer lifetimes for light PBHs.

### C. Near-extremal charged PBHs

The scaling derived above applies to ordinary non-extremal PBHs. A different behaviour may arise for near-extremal charged black holes, because their Hawking temperature is suppressed relative to the Schwarzschild–Tangherlini temperature of a black hole with the same mass. We denote by  $\beta$  the deviation from extremality, with  $\beta \ll 1$  corresponding to a nearly extremal configuration. Compared with the static BH temperature, the near-extremal temperature can be expressed as [15]

$$T_{\text{ne}} \simeq T_0 \sqrt{\frac{\beta}{S_{\text{BH}}}}, \quad (38)$$

where  $T_0$  is the ordinary six-dimensional Schwarzschild–Tangherlini temperature given in Eq. (21), and  $S_{\text{BH}}$  is the corresponding Bekenstein–Hawking entropy given in Eq. (22). Equivalently,

$$\frac{T_0}{T_{\text{ne}}} \simeq \frac{S_{\text{BH}}^{1/2}}{\sqrt{\beta}}. \quad (39)$$

In what follows, we use this temperature suppression as a phenomenological parametrization of the near-extremal lifetime enhancement. Including the memory-burden suppression factor  $S_{\text{BH}}^p$ , we write

$$\tau_{\text{ne}}^{(p)} \sim \frac{S_{\text{BH}}^{p+1/2}}{\sqrt{\beta}} \tau_0, \quad (40)$$

where  $\tau_0$  is the ordinary six-dimensional Schwarzschild–Tangherlini lifetime defined in Eq. (25). This expression should be understood as a phenomenological scaling Ansatz for near-extremal charged PBHs. It should not be used for ordinary non-extremal Schwarzschild–Tangherlini PBHs, nor for generic rotating PBHs after spin-down.

Using the entropy scaling in Eq. (22) and the ordinary lifetime scaling in Eq. (24), Eq. (40) gives

$$\begin{aligned} \tau_{\text{ne}}^{(p)}(M_{\text{BH}}) &\propto \frac{1}{\sqrt{\beta}} \left( \frac{M_{\text{BH}}}{M_*} \right)^{\frac{4}{3}(p+\frac{1}{2})} \frac{1}{M_*} \left( \frac{M_{\text{BH}}}{M_*} \right)^{5/3} \\ &\propto \frac{1}{\sqrt{\beta}} \frac{1}{M_*} \left( \frac{M_{\text{BH}}}{M_*} \right)^{\frac{4p+7}{3}}. \end{aligned} \quad (41)$$

At fixed  $M_*$ , this becomes

$$\tau_{\text{ne}}^{(p)} \propto \beta^{-1/2} M_{\text{BH}}^{(4p+7)/3}. \quad (42)$$

Therefore, within this near-extremal parametrization,

$$p = 0: \quad \tau_{\text{ne}} \propto \beta^{-1/2} M_{\text{BH}}^{7/3}, \quad p = 1: \quad \tau_{\text{ne}} \propto \beta^{-1/2} M_{\text{BH}}^{11/3}, \quad p = 2: \quad \tau_{\text{ne}} \propto \beta^{-1/2} M_{\text{BH}}^5. \quad (43)$$

For illustration, we adopt the following benchmark normalization for near-extremal charged six-dimensional PBHs:

$$\begin{aligned} \tau_{\text{ne}}^{(p=0)}(M_{\text{BH}}) &\simeq \frac{53.5}{\sqrt{\beta}} \left( \frac{M_{\text{BH}}}{\text{g}} \right)^{7/3} \text{Gyr}, \\ \tau_{\text{ne}}^{(p=1)}(M_{\text{BH}}) &\simeq \frac{2.5 \times 10^{27}}{\sqrt{\beta}} \left( \frac{M_{\text{BH}}}{\text{g}} \right)^{11/3} \text{Gyr}, \\ \tau_{\text{ne}}^{(p=2)}(M_{\text{BH}}) &\simeq \frac{1.1 \times 10^{54}}{\sqrt{\beta}} \left( \frac{M_{\text{BH}}}{\text{g}} \right)^5 \text{Gyr}. \end{aligned} \quad (44)$$

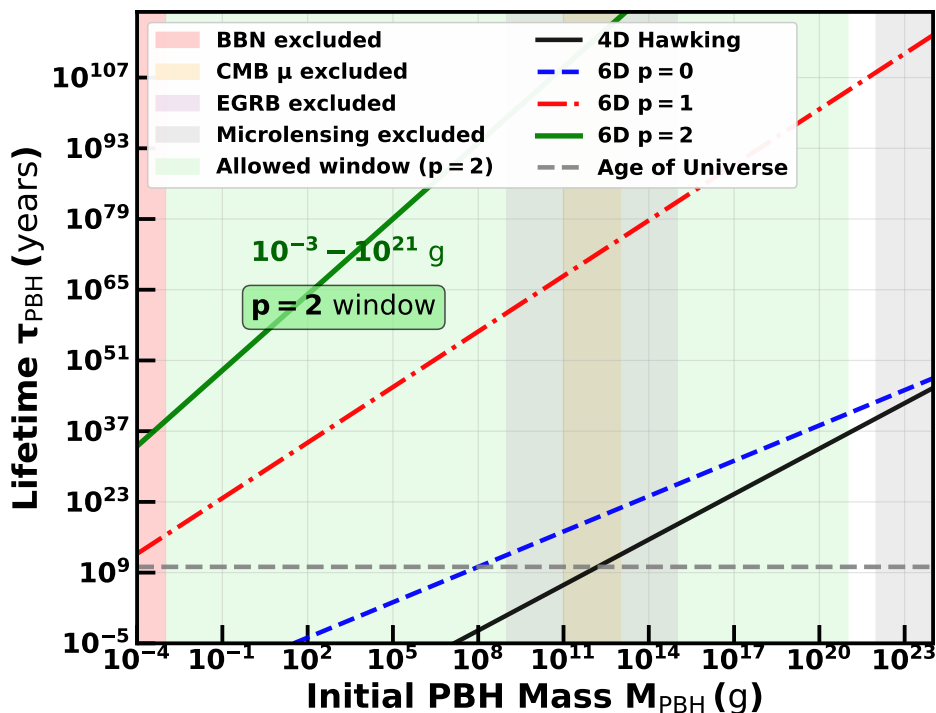


FIG. 1: Lifetime of primordial black holes as a function of the initial PBH mass in four and six dimensions. The black solid curve shows the standard 4d Hawking evaporation result, while the blue dashed, red dash-dotted, and green solid curves correspond to the 6d cases with memory-burden parameters  $p = 0$ ,  $p = 1$ , and  $p = 2$ , respectively. The horizontal grey dashed line marks the age of the Universe (13.8 Gyr). Shaded regions indicate observational constraints from BBN (red), CMB  $\mu$ -distortions (orange), the extragalactic gamma-ray background (purple), and microlensing (grey). The light-green region highlights the viable dark-matter window for the delayed memory-burden scenario ( $p = 2$ ), namely  $10^{-3} \text{ g} \lesssim M_{\text{PBH}} \lesssim 10^{21} \text{ g}$ .

These numerical expressions are model-dependent and apply only to the near-extremal charged PBH scenario. They should not be confused with the ordinary six-dimensional Hawking lifetime in Eq. (25).

Table I summarizes the resulting viable PBH dark-matter windows for representative values of  $\beta$ . As the black hole approaches extremality,  $\beta \ll 1$ , the lifetime is enhanced by the factor  $\beta^{-1/2}$ , and the allowed mass range can extend to smaller masses. Such an extension, however, requires a formation mechanism capable of producing a population of nearly extremal charged PBHs. In the absence of such a mechanism, the near-extremal case should be regarded as an illustrative possibility rather than the conservative baseline.

TABLE I: Illustrative lower mass bounds for six-dimensional PBH dark matter. The column labelled  $p = 0$  corresponds to the standard Hawking evaporation case, while the column labelled  $p = 2$  includes the memory-burden enhancement. The entries for  $p = 2$  should be understood as conservative phenomenological lower limits, including the expected effect of pre-burden energy injection and BBN constraints. The parameter  $\beta$  denotes the deviation from extremality;  $\beta = 1$  corresponds to the ordinary non-extremal limit, while  $\beta \ll 1$  corresponds to a near-extremal charged configuration.

$\beta$ ↓	Standard evaporation $p = 0$	Memory-burdened evaporation $p = 2$
1	$M_{\text{BH}} \gtrsim 10^8 \text{ g}$	$M_{\text{BH}} \gtrsim 10^{-3} \text{ g}$
$10^{-4}$	$M_{\text{BH}} \gtrsim 10^6 \text{ g}$	$M_{\text{BH}} \gtrsim 10^{-4} \text{ g}$
$10^{-8}$	$M_{\text{BH}} \gtrsim 10^4 \text{ g}$	$M_{\text{BH}} \gtrsim 10^{-5} \text{ g}$

#### D. Energy-injection constraints and the viable dark-matter window

The viability of a PBH population as dark matter rests on two basic requirements. First, the individual black holes must survive until the present epoch. Second, their evaporative emission must not violate observational bounds on energy injection during BBN, the CMB  $\mu$ -distortion era, or the later diffuse gamma-ray background. In the memory-burdened picture, the evaporation history separates into a short pre-burden phase, during which the PBH evaporates approximately at the standard Hawking rate, and a much longer post-burden phase in which the emission rate is suppressed. The relevant scaling laws differ for ordinary non-extremal six-dimensional PBHs and for near-extremal charged PBHs, which have an additional temperature suppression.

**Ordinary non-extremal six-dimensional PBHs.** For an ordinary non-extremal black hole that has spun down to a Schwarzschild–Tangherlini configuration, the memory-burdened lifetime was derived in Eq. (35). Equivalently,

$$\tau_{\text{MB}}^{(p)}(M_{\text{BH}}) \propto M_{\text{BH}}^{(4p+5)/3} M_*^{-(4p+8)/3}. \quad (45)$$

At fixed  $M_*$ , this gives

$$p = 0: \quad \tau \propto M_{\text{BH}}^{5/3}, \quad p = 1: \quad \tau \propto M_{\text{BH}}^3, \quad p = 2: \quad \tau \propto M_{\text{BH}}^{13/3}. \quad (46)$$

The post-burden luminosity is suppressed by one entropy factor for each power of the memory exponent,

$$L_{\text{MB}}^{(p)} \sim L_{\text{std}} S_{\text{BH}}^{-p}, \quad (47)$$

where  $L_{\text{std}}$  is the standard six-dimensional Hawking luminosity at the same mass and  $S_{\text{BH}}$  is the Bekenstein–Hawking entropy.

**Near-extremal charged six-dimensional PBHs.** For a charged black hole close to extremality, the Hawking temperature is further reduced relative to the Schwarzschild–Tangherlini temperature. Using the near-extremal parametrization introduced in Eq. (38), and including the memory-burden factor, the lifetime scales as derived in Eq. (41):

$$\tau_{\text{ne}}^{(p)}(M_{\text{BH}}) \propto \beta^{-1/2} M_{\text{BH}}^{(4p+7)/3} M_*^{-(4p+10)/3}. \quad (48)$$

At fixed  $M_*$ , this becomes

$$p = 0: \quad \tau_{\text{ne}} \propto \beta^{-1/2} M_{\text{BH}}^{7/3}, \quad p = 1: \quad \tau_{\text{ne}} \propto \beta^{-1/2} M_{\text{BH}}^{11/3}, \quad p = 2: \quad \tau_{\text{ne}} \propto \beta^{-1/2} M_{\text{BH}}^5. \quad (49)$$

Consistently with the same phenomenological temperature and entropy suppression, the post-burden luminosity may be estimated as

$$L_{\text{ne}}^{(p)} \sim L_{\text{std}} \frac{\sqrt{\beta}}{S_{\text{BH}}^{p+1/2}}. \quad (50)$$

This near-extremal scaling should not be interpreted as the ordinary non-extremal limit at  $\beta = 1$ . It applies only to the charged near-extremal regime.

**Quantitative comparison:  $p = 1$  versus  $p = 2$ .** To estimate the size of the post-burden emission, consider a representative PBH mass

$$M_{\text{BH}} = 10^{11} \text{ g}.$$

Using the reference six-dimensional lifetime normalization in Eq. (25), with  $M_* \simeq 10$  TeV, one obtains

$$\tau_0(10^{11} \text{ g}) \simeq 1.37 \times 10^6 \text{ Gyr}.$$

The corresponding standard luminosity is roughly

$$L_{\text{std}} \sim \frac{M_{\text{BH}} c^2}{\tau_0} \approx 2 \times 10^9 \text{ erg/s}. \quad (51)$$

The six-dimensional entropy is

$$S_{\text{BH}} \sim \left( \frac{M_{\text{BH}}}{M_*} \right)^{4/3} \approx 10^{41}, \quad M_* \simeq 10 \text{ TeV} \simeq 1.78 \times 10^{-20} \text{ g}. \quad (52)$$

TABLE II: Luminocities for ordinary non-extremal, and near-extremal Primordial Black Holes

	Ordinary non-extremal	Near-extremal reference
$p = 1$	$L_{\text{MB}}^{(1)} \sim 10^{-32} \text{ erg/s}$	$L_{\text{ne}}^{(1)} \sim 10^{-52} \sqrt{\beta} \text{ erg/s}$
$p = 2$	$L_{\text{MB}}^{(2)} \sim 10^{-73} \text{ erg/s}$	$L_{\text{ne}}^{(2)} \sim 10^{-93} \sqrt{\beta} \text{ erg/s}$

Substituting these values into Eqs. (47) and (50) gives the order-of-magnitude estimates presented in Table II.

Even the largest of these post-burden luminosities is negligible on cosmological scales. Therefore, the dominant phenomenological constraint does not come from the late post-burden luminosity itself, but from the short pre-burden phase, during which the PBH still evaporates approximately at the standard Hawking rate. The relevant energy-injection bound is then controlled by the amount of energy emitted before the memory burden becomes effective, rather than by the highly suppressed post-burden luminosity.

**Pre-burden energy injection and the status of the  $p = 1$  scenario.** Before the memory burden becomes effective, the black hole loses a fractional mass through approximately standard Hawking radiation. Associated with this, we introduce the following definition

$$q \equiv \frac{\Delta M_{\text{crit}}}{M_0} \quad (53)$$

Using the onset criterion in Eq. (32), one has

$$q \sim [p S_{\text{BH}}(M_0)]^{-1/p},$$

where  $M_0$  is the initial PBH mass. Therefore,

$$p = 1 : \quad q \sim S_{\text{BH}}^{-1}, \quad p = 2 : \quad q \sim (2S_{\text{BH}})^{-1/2}. \quad (54)$$

For macroscopic black holes,  $S_{\text{BH}} \gg 1$ , so the fractional mass loss before the onset of the burden is small.

For example, for  $M_0 = 10^{11} \text{ g}$  and  $M_* \simeq 10 \text{ TeV}$ , Eq. (52) gives

$$S_{\text{BH}}(M_0) \sim 10^{41}.$$

Thus, for  $p = 1$ ,

$$q \sim 10^{-41}, \quad \Delta E_{\text{pre}} \sim q M_0 c^2 \sim 10^{-9} \text{ erg}, \quad (55)$$

which is negligible per black hole. For  $p = 2$ , the onset fraction is larger,

$$q \sim (2 \times 10^{41})^{-1/2} \sim 10^{-21},$$

but it is still extremely small compared with unity.

The smallness of the pre-burden fractional mass loss does not by itself guarantee that the  $p = 1$  scenario is automatically safe. After the onset of the burden, the ordinary non-extremal luminosity is suppressed only by one entropy factor,  $S_{\text{BH}}^{-1}$ , whereas for  $p = 2$  it is suppressed by  $S_{\text{BH}}^{-2}$ . Consequently, the  $p = 1$  case is more sensitive to the precise onset prescription, the emitted spectrum, the PBH abundance, and the redshift at which the emission occurs. A dedicated redshift-dependent energy-injection calculation is therefore required before a robust  $p = 1$  dark-matter window can be claimed.

For near-extremal charged PBHs with  $p = 1$ , the additional temperature suppression reduces the post-burden luminosity further, as shown in Eq. (50). However, the onset of the burden and the cosmological impact of the pre-burden emission may depend on the near-extremality parameter  $\beta$ , the formation mechanism, and the PBH abundance. We therefore treat the  $p = 1$  near-extremal case as a possible but model-dependent extension, rather than as the conservative baseline. By contrast, the  $p = 2$  scenario is more robust because its post-burden luminosity is suppressed by an additional power of the entropy.

**Phenomenological lower bound from the pre-burden phase for  $p = 2$ .** Even for  $p = 2$ , the pre-burden phase can impose a lower limit on the PBH mass. Taking the benchmark value

$$M_* \simeq 10 \text{ TeV} \simeq 1.78 \times 10^{-20} \text{ g},$$

and using the entropy scaling in Eq. (22), one finds for  $M_{\text{BH}} = 10^{-3} \text{ g}$

$$S_{\text{BH}} \sim \left( \frac{10^{-3}}{1.78 \times 10^{-20}} \right)^{4/3} \approx 2 \times 10^{22}. \quad (56)$$

For  $p = 2$ , the critical fractional mass loss is therefore

$$q \sim (2S_{\text{BH}})^{-1/2} \approx 5 \times 10^{-12}. \quad (57)$$

The corresponding pre-burden energy release per PBH is

$$\Delta E_{\text{pre}} \simeq q M_{\text{BH}} c^2 \approx 5 \times 10^{-12} \times 10^{-3} \text{ g} \times 9 \times 10^{20} \text{ erg/g} \approx 4.5 \times 10^6 \text{ erg}. \quad (58)$$

For  $p = 2$ , the onset fraction scales as

$$q \propto S_{\text{BH}}^{-1/2} \propto M_{\text{BH}}^{-2/3}. \quad (59)$$

Thus, smaller PBHs lose a larger fraction of their mass before the memory burden becomes effective. The energy released per individual PBH scales as

$$\Delta E_{\text{pre}} \sim q M_{\text{BH}} c^2 \propto M_{\text{BH}}^{1/3},$$

whereas the injected energy density at fixed dark-matter fraction scales as

$$\rho_{\text{inj}}^{\text{pre}} \sim q \rho_{\text{PBH}} c^2 \propto M_{\text{BH}}^{-2/3}.$$

Therefore, the cosmological impact of the pre-burden phase becomes more important for lighter PBHs even though the energy released by each individual PBH decreases.

The precise lower bound cannot be obtained from the energy per black hole alone. It requires the PBH abundance, the emitted particle spectrum, the redshift of emission, and the relevant BBN, CMB  $\mu$ -distortion, and diffuse-background energy-injection bounds. Nevertheless, for a PBH population making up all of the dark matter, we adopt

$$M_{\text{min}} \sim 10^{-3} \text{ g} \quad (60)$$

as a conservative phenomenological lower edge in the  $p = 2$  memory-burdened scenario.

**Resulting dark-matter windows.** Combining the survival requirement with the expected constraints from pre-burden energy injection, BBN, CMB  $\mu$ -distortions, the diffuse gamma-ray background, and compact-object searches, we obtain the conservative mass interval summarized in Table III. For the ordinary non-extremal  $p = 2$  scenario, the viable baseline window is taken to be

$$10^{-3} \text{ g} \lesssim M_{\text{PBH}} \lesssim 10^{21} \text{ g}. \quad (61)$$

The lower edge is phenomenological and is controlled by pre-burden energy injection, while the upper edge is set by the usual compact-object dark-matter constraints, especially microlensing. Near-extremal charged PBHs can have even longer lifetimes because of the additional  $\beta^{-1/2}$  enhancement, but such scenarios require a formation mechanism capable of producing a near-extremal PBH population. We therefore treat them as illustrative extensions rather than as the baseline dark-matter window.

TABLE III: Conservative PBH dark-matter windows in the six-dimensional scenario for  $f_{\text{PBH}} = 1$ .

Scenario	Standard evaporation, $p = 0$	Memory burden, $p = 2$
Ordinary non-extremal	$M_{\text{PBH}} \gtrsim 10^8 \text{ g}$	$10^{-3} \text{ g} \lesssim M_{\text{PBH}} \lesssim 10^{21} \text{ g}$
Near-extremal charged, $\beta \ll 1$	Enhanced by $\beta^{-1/2}$	Formation-dependent extension

Thus the ordinary non-extremal  $p = 2$  memory-burdened scenario provides a conservative broad PBH dark-matter window. Near-extremality can extend the lifetime further, but the corresponding mass range is not quoted as a model-independent bound because it depends on the charge distribution, the value of  $\beta$ , and the formation mechanism.

### E. The Festina–Lente bound and near-extremal charged PBHs

The preceding discussion of near-extremal charged PBHs raises an important consistency question: can the electric field of a nearly extremal black hole be made arbitrarily small, corresponding to  $\beta \rightarrow 0$ , without conflicting with quantum-gravity constraints? In de Sitter space, the Festina–Lente (FL) bound provides a criterion for whether charged particles are sufficiently light to allow efficient Schwinger discharge of near-extremal charged black holes [60, 61]. Parametrically, the bound requires the existence of charged states light enough that Schwinger pair production is not exponentially suppressed in the relevant background field. In four-dimensional notation this is often written, up to order-one factors, as an upper bound of the form

$$m^2 \lesssim qg H M_{\text{Pl}}. \quad (62)$$

In higher dimensions the precise expression depends on the normalization of the gauge coupling, the Planck scale, and the near-Nariai geometry. Below we use the FL bound only as a consistency check on the near-extremal charged PBH interpretation; it is not needed for the ordinary non-extremal  $p = 2$  memory-burdened dark-matter window.

#### 1. The Nariai limit in $d$ dimensions

Consider the  $d$ -dimensional Reissner–Nordström–de Sitter (RNdS) geometry [62, 63],

$$ds^2 = -U(r)dt^2 + \frac{dr^2}{U(r)} + r^2 d\Omega_{d-2}^2, \quad (63)$$

with

$$U(r) = 1 - \frac{\mu}{r^{d-3}} + \frac{Q_d^2}{r^{2d-6}} - \frac{r^2}{\ell^2}, \quad (64)$$

where

$$\mu \equiv \frac{2M}{M_P^{d-2}}, \quad Q_d^2 \equiv \frac{g^2 q^2}{4\pi M_P^{d-2}}. \quad (65)$$

Here  $M$  is the black-hole mass,  $q$  is the charge quantum number,  $g$  is the gauge coupling,  $M_P$  is the  $d$ -dimensional Planck scale, and  $\ell$  is the de Sitter radius.

The Nariai limit corresponds to the degeneracy of the black-hole and cosmological horizons [63, 64]. At the degenerate horizon  $r = r_N$ , one has

$$U(r_N) = 0, \quad U'(r_N) = 0. \quad (66)$$

It is useful to define

$$n \equiv d - 3. \quad (67)$$

Then

$$U(r) = 1 - \frac{\mu}{r^n} + \frac{Q_d^2}{r^{2n}} - \frac{r^2}{\ell^2}. \quad (68)$$

The derivative is

$$U'(r) = \frac{n\mu}{r^{n+1}} - \frac{2nQ_d^2}{r^{2n+1}} - \frac{2r}{\ell^2}. \quad (69)$$

Imposing  $U'(r_N) = 0$  gives

$$\frac{\mu}{r_N^n} = 2 \frac{Q_d^2}{r_N^{2n}} + \frac{2}{n} \frac{r_N^2}{\ell^2}. \quad (70)$$

Substituting this into  $U(r_N) = 0$ , we obtain

$$0 = 1 - \frac{Q_d^2}{r_N^{2n}} - \left(1 + \frac{2}{n}\right) \frac{r_N^2}{\ell^2}. \quad (71)$$

Therefore,

$$\frac{Q_d^2}{r_N^{2n}} = 1 - \frac{n+2}{n} \frac{r_N^2}{\ell^2}. \quad (72)$$

Restoring  $n = d - 3$ , this becomes

$$\frac{Q_d^2}{r_N^{2d-6}} = 1 - \frac{d-1}{d-3} \frac{r_N^2}{\ell^2} \quad (73)$$

or, in terms of the original charge parameter,

$$\frac{g^2 q^2}{4\pi M_P^{d-2} r_N^{2d-6}} = 1 - \frac{d-1}{d-3} \frac{r_N^2}{\ell^2}. \quad (74)$$

The mass parameter is obtained from Eq. (70):

$$\frac{\mu}{r_N^n} = 2 - 2 \frac{n+1}{n} \frac{r_N^2}{\ell^2}. \quad (75)$$

Thus,

$$M = M_P^{d-2} r_N^{d-3} \left[ 1 - \frac{d-2}{d-3} \frac{r_N^2}{\ell^2} \right]. \quad (76)$$

Equations (74) and (76) show that, for charged RNdS black holes, the Nariai radius is not fixed uniquely by  $d$  and  $\ell$ . Instead,  $r_N$  parametrizes a family of charged Nariai solutions. The charge relation implies

$$\frac{r_N^2}{\ell^2} \leq \frac{d-3}{d-1}. \quad (77)$$

The equality corresponds to the neutral Nariai limit  $q = 0$ , for which

$$r_N^2 = \frac{d-3}{d-1} \ell^2. \quad (78)$$

For nonzero charge,  $q \neq 0$ , the left-hand side of Eq. (74) is strictly positive. Consequently,  $1 - \frac{d-1}{d-3} \frac{r_N^2}{\ell^2} > 0$ , which implies  $\frac{r_N^2}{\ell^2} < \frac{d-3}{d-1}$ , or equivalently  $r_N < \ell \sqrt{(d-3)/(d-1)} = r_N^{(q=0)}$ . Hence, the Nariai radius of a charged solution is strictly smaller than its neutral value and is determined by Eq. (74).

## 2. Electric field on the Nariai horizon

The discharge of a charged near-Nariai black hole proceeds through Schwinger pair production in the background electric field [60, 65, 66]. With the same normalization used in Eq. (64), we define

$$Q_d^2 \equiv \frac{g^2 q^2}{4\pi M_P^{d-2}}, \quad (79)$$

so that the electric field may be written as

$$E(r) = \frac{Q_d}{2\sqrt{\pi} r^{d-2}}. \quad (80)$$

At the Nariai horizon,

$$E_N = \frac{Q_d}{2\sqrt{\pi} r_N^{d-2}}. \quad (81)$$

Using the charge–radius relation derived in Eq. (73), the Nariai charge parameter is

$$Q_d = r_N^{d-3} \left[ 1 - \frac{d-1}{d-3} \frac{r_N^2}{\ell^2} \right]^{1/2}. \quad (82)$$

Substituting this into Eq. (81) gives

$$E_N = \frac{1}{2\sqrt{\pi} r_N} \left[ 1 - \frac{d-1}{d-3} \frac{r_N^2}{\ell^2} \right]^{1/2}. \quad (83)$$

Equivalently, defining

$$x_N \equiv \frac{r_N}{\ell}, \quad H \equiv \ell^{-1}, \quad (84)$$

$E_N$  can be re-written as follows:

$$E_N = \frac{H}{2\sqrt{\pi} x_N} \left[ 1 - \frac{d-1}{d-3} x_N^2 \right]^{1/2}, \quad (85)$$

which for  $d = 6$ , takes the form

$$E_N^{(6)} = \frac{H}{2\sqrt{\pi} x_N} \left( 1 - \frac{5}{3} x_N^2 \right)^{1/2}, \quad 0 < x_N^2 \leq \frac{3}{5}. \quad (86)$$

Thus the Nariai electric field is not fixed solely by the spacetime dimension. It depends on the charged Nariai branch through  $x_N = r_N/\ell$ . In the neutral Nariai limit,  $x_N^2 = (d-3)/(d-1)$ , the electric field correctly vanishes.

### 3. Schwinger pair production and the Festina–Lente bound

In a locally constant electric field  $E$ , the Schwinger pair-production rate for a particle of mass  $m$  and physical charge  $e_{\text{phys}}$  has the schematic form [65]

$$\Gamma_{\text{Schw}} \sim \frac{(e_{\text{phys}} E)^{d/2}}{(2\pi)^{d-1}} \exp \left[ -\frac{\pi m^2}{e_{\text{phys}} E} \right], \quad (87)$$

up to spin-dependent, curvature-dependent, and geometry-dependent prefactors, the Schwinger exponent separates two parametric regimes:

$$\frac{\pi m^2}{e_{\text{phys}} E_N} \begin{cases} \lesssim 1, & \text{efficient Schwinger discharge,} \\ \gtrsim 1, & \text{exponentially suppressed discharge (FL regime).} \end{cases} \quad (88)$$

Thus, avoiding rapid Schwinger discharge of charged Nariai black holes requires parametrically  $m^2 \gtrsim e_{\text{phys}} E_N/\pi$ , up to order-one corrections. This constitutes the physical content of the Festina–Lente bound [60, 61]. In  $d$  spacetime dimensions, the FL bound can be written, up to order-one numerical factors, as

$$m^2 \gtrsim g_D q \left[ \frac{(d-1)(d-2)}{2} \right]^{1/2} M_D^{(d-2)/2} H, \quad (89)$$

or equivalently

$$m \gtrsim (g_D q)^{1/2} \left[ \frac{(d-1)(d-2)}{2} \right]^{1/4} M_D^{(d-2)/4} H^{1/2}. \quad (90)$$

Thus the FL condition is a lower bound on the mass of charged states. For the two-dark-dimensions scenario,  $d = 6$ ,  $M_D = M_6 = M_*$ , and the six-dimensional gauge coupling has mass dimension

$$[g_6] = -1. \quad (91)$$

Equation (90) then gives

$$m \gtrsim (g_6 q)^{1/2} 10^{1/4} M_* H^{1/2}. \quad (92)$$

If a charged field propagates in the six-dimensional bulk, its six-dimensional gauge coupling is related to the four-dimensional coupling by

$$e = \frac{g_6}{\sqrt{V_2}} = \frac{g_6}{2\pi R}, \quad g_6 = e(2\pi R). \quad (93)$$

Using the compactification relation in Eq. (12), one obtains

$$(g_6 q)^{1/2} = (eq)^{1/2} \frac{M_{\text{Pl}}^{1/2}}{M_*}. \quad (94)$$

Substituting this into Eq. (92) gives

$$m \gtrsim (eq)^{1/2} 10^{1/4} (M_{\text{Pl}} H)^{1/2}. \quad (95)$$

This is the useful four-dimensional form of the six-dimensional FL condition after dimensional reduction.

For  $q = 1$ ,  $e \simeq 0.3$ , and  $M_{\text{Pl}} = 2.4 \times 10^{18}$  GeV, Eq. (95) becomes

$$m \gtrsim 1.5 \times 10^{16} \text{ GeV} \left( \frac{H}{10^{14} \text{ GeV}} \right)^{1/2}, \quad (96)$$

up to order-one geometric factors. This scale is vastly larger than the KK mass gap. Therefore, if electrically charged Standard Model fields were allowed to propagate in the bulk during a high-scale de Sitter phase, their light KK excitations would violate the FL criterion. This provides additional motivation for localizing charged Standard Model fields on the brane, or alternatively for requiring a much lower inflationary Hubble scale.

For the present de Sitter epoch,

$$H_0 \simeq 1.5 \times 10^{-42} \text{ GeV}, \quad (97)$$

Eq. (95) gives

$$m \gtrsim 2 \times 10^{-3} \text{ eV}, \quad (98)$$

again up to order-one factors. Thus the present-day FL bound is mild for ordinary charged Standard Model particles, but it can constrain ultralight charged states.

Figure 2 illustrates the charged Nariai structure in the six-dimensional case. The left panel shows how the black-hole and cosmological horizons merge in the Nariai limit, while a small deformation away from this limit splits the degenerate horizon into separate horizons. The right panel shows the corresponding electric field on the charged Nariai branch. Unlike the neutral Nariai radius, the charged Nariai electric field is not fixed only by the spacetime dimension; it depends on the branch parameter  $x_N = r_N/\ell$ . This is why the FL bound should be applied as a consistency condition on charged states rather than as a universal fixed numerical bound on the near-extremality parameter.

We emphasize, however, that the FL bound does not give a model-independent constraint on the near-extremality parameter  $\beta$  of a primordial black hole. Such a bound would require the explicit charged black-hole solution, the relation between  $\beta$  and the horizon electric field, and the spectrum of charged particles available for Schwinger discharge. Therefore, in this work we use the FL bound only as a consistency check on charged bulk states. It does not modify the conservative ordinary non-extremal  $p = 2$  PBH dark-matter window discussed above.

#### IV. SCALAR-INDUCED GRAVITATIONAL WAVES IN THE 6D SCENARIO

Primordial black holes are produced when large curvature perturbations generated during inflation re-enter the Hubble horizon in the radiation-dominated epoch and undergo gravitational collapse [20, 21]. A perturbation mode with comoving wavenumber  $k$  re-enters the horizon when  $k = aH$ . The mass of the resulting black hole is approximately a fraction  $\gamma$  of the horizon mass at that time,

$$M_{\text{PBH}} \simeq \gamma M_H = \gamma \frac{4\pi}{3} \rho H^{-3} \Big|_{\text{re-entry}}, \quad (99)$$

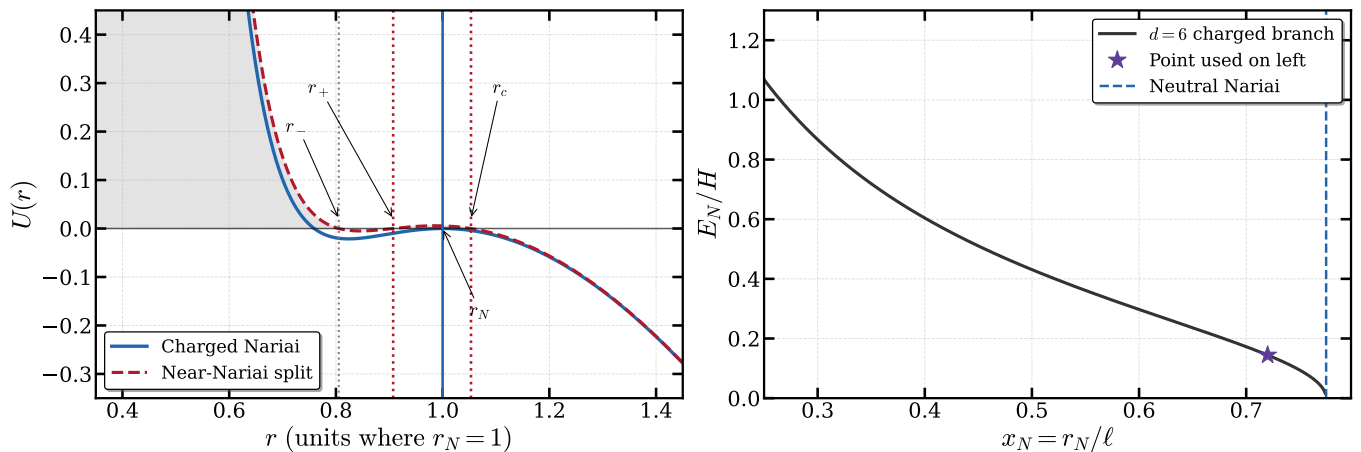


FIG. 2: Illustration of the charged Nariai limit in six-dimensional Reissner–Nordström–de Sitter geometry. Left: metric function  $U(r)$  for the charged Nariai solution and a near-Nariai split. In the Nariai limit the black-hole and cosmological horizons merge at the degenerate radius  $r_N$ , while the near-Nariai solution displays separated horizons  $r_+$  and  $r_c$ , together with the inner horizon  $r_-$ . Right: electric field on the charged Nariai horizon, normalized by the de Sitter scale  $H = \ell^{-1}$ , as a function of  $x_N = r_N/\ell$  for  $d = 6$ . The electric field is not a universal constant times  $H$ ; it depends on the charged Nariai branch and vanishes at the neutral Nariai endpoint  $x_N^2 = 3/5$ .

where  $\gamma \simeq 0.2$  characterizes the collapse efficiency. During radiation domination,  $\rho = 3M_{\text{Pl}}^2 H^2$ , so

$$M_{\text{PBH}} \simeq 4\pi\gamma \frac{M_{\text{Pl}}^2}{H_{\text{form}}}. \quad (100)$$

Using entropy conservation, the PBH mass is related to the comoving scale by

$$M_{\text{PBH}}(k) \simeq 10^{18} \text{ g} \left(\frac{\gamma}{0.2}\right) \left(\frac{g_*}{106.75}\right)^{-1/6} \left(\frac{k}{7 \times 10^{13} \text{ Mpc}^{-1}}\right)^{-2}. \quad (101)$$

Equivalently,

$$k \simeq 7 \times 10^{13} \text{ Mpc}^{-1} \left(\frac{\gamma}{0.2}\right)^{1/2} \left(\frac{g_*}{106.75}\right)^{-1/12} \left(\frac{M_{\text{PBH}}}{10^{18} \text{ g}}\right)^{-1/2}. \quad (102)$$

The corresponding present-day frequency is

$$f \simeq 0.11 \text{ Hz} \left(\frac{\gamma}{0.2}\right)^{1/2} \left(\frac{g_*}{106.75}\right)^{-1/12} \left(\frac{M_{\text{PBH}}}{10^{18} \text{ g}}\right)^{-1/2}. \quad (103)$$

The primordial curvature power spectrum is modelled as a log-normal enhancement at the scale  $k_*$  corresponding to the characteristic PBH mass  $M_{\text{PBH}}$  [28, 67, 68]:

$$\mathcal{P}_{\mathcal{R}}(k) = \frac{A_{\mathcal{R}}}{\sqrt{2\pi}\sigma_k} \exp\left[-\frac{\ln^2(k/k_*)}{2\sigma_k^2}\right], \quad (104)$$

where  $A_{\mathcal{R}}$  sets the integrated power and  $\sigma_k$  controls the logarithmic width of the peak. For the PBH abundance we use a phenomenological log-normal mass function per logarithmic mass interval,

$$\frac{df_{\text{PBH}}}{d \ln M} = \frac{f_{\text{PBH}}}{\sqrt{2\pi}\sigma_M} \exp\left[-\frac{\ln^2(M/M_p)}{2\sigma_M^2}\right], \quad (105)$$

which satisfies

$$\int d \ln M \frac{df_{\text{PBH}}}{d \ln M} = f_{\text{PBH}}. \quad (106)$$

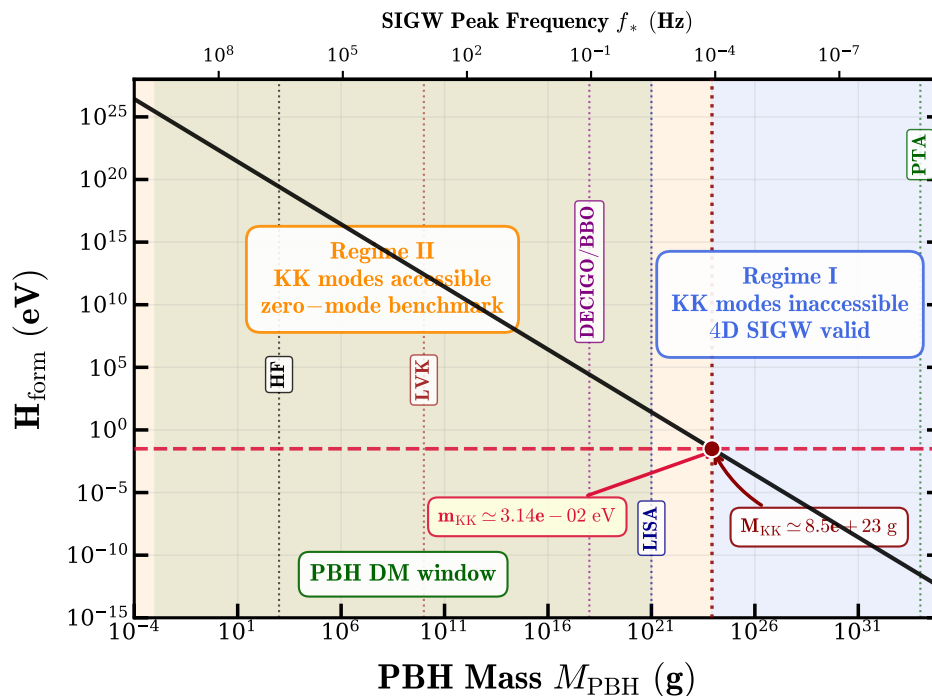


FIG. 3: Regimes of validity for scalar-induced gravitational waves in the six-dimensional two-dark-dimensions scenario. The black curve shows the Hubble scale at PBH formation,  $H_{\text{form}}$ , as a function of the PBH mass. The horizontal dashed line denotes the KK mass gap  $m_{\text{KK}}$ . For  $M_{\text{PBH}} > M_{\text{KK}}$ , massive KK gravitons are kinematically inaccessible and the standard four-dimensional SIGW formalism is a valid effective description. For  $M_{\text{PBH}} < M_{\text{KK}}$ , the KK tower is accessible and the 4D SIGW spectrum should be interpreted as a zero-mode benchmark rather than the complete six-dimensional prediction. The green shaded region indicates the memory-burdened PBH dark-matter window.

Equivalently, if one defines

$$\psi(M) \equiv \frac{df_{\text{PBH}}}{dM}, \quad (107)$$

then

$$\psi(M) = \frac{f_{\text{PBH}}}{\sqrt{2\pi} \sigma_M M} \exp\left[-\frac{\ln^2(M/M_p)}{2\sigma_M^2}\right], \quad (108)$$

so that  $\int dM \psi(M) = f_{\text{PBH}}$ .

In this work we use the log-normal mass function as a phenomenological description of the PBH population. We consider representative benchmarks with  $f_{\text{PBH}} = 1$ . A broad benchmark with  $\sigma_M = 1$  and  $M_p = 10^{10}$  g corresponds to very high frequencies,  $f \sim 10^3$  Hz. The memory-burdened lower edge,  $M_p = 10^{-3}$  g, corresponds to GHz frequencies and is therefore far above the standard LISA/DECIGO/BBO/PTA bands. Masses in the range  $M_p \sim 10^{18}$ – $10^{21}$  g correspond instead to the deci-Hz to mHz bands relevant for future space-based gravitational-wave observatories.

### A. Regimes of validity

The standard scalar-induced gravitational-wave calculation assumes a four-dimensional massless tensor sector. In the present six-dimensional scenario this approximation must be checked against the KK mass gap. At horizon re-entry, the physical momentum of the scalar mode is of order the Hubble scale,  $k/a \simeq H_{\text{form}}$ . Therefore massive KK tensor modes can be kinematically excited only if

$$H_{\text{form}} \gtrsim m_{\text{KK}}. \quad (109)$$

This condition separates the parameter space into a four-dimensional regime and a KK-sensitive regime. Using the PBH mass–Hubble relation in Eq. (100), the formation scale can be written as

$$H_{\text{form}} \simeq 4\pi\gamma \frac{M_{\text{Pl}}^2}{M_{\text{PBH}}}, \quad (110)$$

where  $M_{\text{Pl}}$  denotes the reduced Planck mass. With the reduced-length convention  $L = 2\pi R$ , the KK threshold used in this work is

$$m_{\text{KK}} = \frac{1}{L} = \frac{1}{2\pi R} \simeq 3.1 \times 10^{-2} \text{ eV}. \quad (111)$$

Combining Eqs. (109)–(111), the boundary mass is

$$M_{\text{KK}} \equiv 4\pi\gamma \frac{M_{\text{Pl}}^2}{m_{\text{KK}}} \simeq 8.5 \times 10^{23} \text{ g} \left( \frac{\gamma}{0.2} \right) \left( \frac{3.1 \times 10^{-2} \text{ eV}}{m_{\text{KK}}} \right). \quad (112)$$

Equivalently, using the mass–frequency relation in Eq. (103), this corresponds to

$$f_{\text{KK}} \simeq 1.2 \times 10^{-4} \text{ Hz}. \quad (113)$$

We therefore distinguish two regimes:

- **Regime I:**  $M_{\text{PBH}} \gtrsim M_{\text{KK}}$ , or equivalently  $f_* \lesssim f_{\text{KK}}$ . In this case  $H_{\text{form}} \lesssim m_{\text{KK}}$ , so the massive KK tower is not kinematically accessible. The usual four-dimensional SIGW formalism is then a self-consistent effective description [25, 26, 37].
- **Regime II:**  $M_{\text{PBH}} \lesssim M_{\text{KK}}$ , or equivalently  $f_* \gtrsim f_{\text{KK}}$ . In this case  $H_{\text{form}} \gtrsim m_{\text{KK}}$ , so massive KK tensor modes can in principle be excited. The four-dimensional SIGW spectrum should then be interpreted as the massless zero-mode benchmark rather than the full six-dimensional prediction.

The memory-burdened PBH dark-matter window considered in this work,

$$10^{-3} \text{ g} \lesssim M_{\text{PBH}} \lesssim 10^{21} \text{ g}, \quad (114)$$

lies entirely below  $M_{\text{KK}} \simeq 8.5 \times 10^{23} \text{ g}$ . Therefore these PBH masses belong to Regime II, and the spectra shown for this window should be read as zero-mode benchmarks. A complete six-dimensional prediction would require the massive tensor Green functions, brane-to-bulk overlap coefficients, massive-mode transfer functions, and detector response to massive tensor polarizations [69–72].

By contrast, PTA-band SIGWs correspond to much smaller frequencies and therefore to much larger PBH masses. For example,  $f_* \sim 10^{-9} \text{ Hz}$  corresponds to  $M_{\text{PBH}} \sim 10^{34} \text{ g}$ , which is far above  $M_{\text{KK}}$ . PTA-band SIGWs therefore lie in Regime I, where the standard four-dimensional SIGW calculation is self-consistent [73, 74].

## B. Full six-dimensional tensor dynamics

In the six-dimensional theory the tensor perturbation decomposes into a massless four-dimensional zero mode  $h_{ij}^{(0)}$  and a tower of massive KK tensor modes  $h_{ij}^{(\vec{n})}$  [48, 49, 75, 76], with

$$m_{\vec{n}} = m_{\text{KK}} \sqrt{n_1^2 + n_2^2}, \quad \vec{n} = (n_1, n_2). \quad (115)$$

At the level of the four-dimensional effective theory, each KK mode obeys a massive tensor equation of the schematic form [69–71],

$$h_{\vec{n}}^{\lambda\prime\prime} + 2\mathcal{H}h_{\vec{n}}^{\lambda\prime} + (k^2 + a^2 m_{\vec{n}}^2) h_{\vec{n}}^{\lambda} = S_{\vec{n}}^{\lambda}(k, \eta), \quad (116)$$

where  $S_{\vec{n}}^{\lambda}$  denotes the projection of the quadratic scalar source onto the corresponding KK wavefunction. This projection contains a model-dependent overlap coefficient, denoted here by  $\mathcal{C}_{\vec{n}}$ . The solution can be written formally in terms of the massive Green function  $G_{\vec{n}}(k; \eta, \tilde{\eta})$ , which then determines the tensor power spectrum  $\mathcal{P}_h^{(\vec{n})}(k, \eta)$ .

The zero mode,  $\bar{n} = 0$ , is massless and reproduces the standard four-dimensional scalar-induced gravitational-wave result [25, 26, 37, 77]. Using the log-normal curvature spectrum from Eq (104) the present-day zero-mode spectrum is

$$\Omega_{\text{GW},0}^{(0)}(k) = \frac{\Omega_{r,0}}{24} \left( \frac{g_{*,0}}{g_{*,c}} \right)^{1/3} \int_0^\infty dv \int_{|1-v|}^{1+v} du \mathcal{K}(u,v) \overline{I^2(u,v)} \times \mathcal{P}_{\mathcal{R}}(ku) \mathcal{P}_{\mathcal{R}}(kv), \quad (117)$$

where  $\mathcal{K}(u,v)$  is the standard scalar-induced tensor kernel and  $\overline{I^2(u,v)}$  is the radiation-era time-averaged kernel [25, 26, 37]. For a massive KK mode, the corresponding expression is modified by the massive Green function and by the overlap with the source. Schematically one may write

$$\Omega_{\text{GW},0}^{(\bar{n})}(k) \sim \frac{\Omega_{r,0}}{24} \left( \frac{g_{*,0}}{g_{*,c}} \right)^{1/3} \int_0^\infty dv \int_{|1-v|}^{1+v} du \mathcal{K}(u,v) \mathcal{C}_{\bar{n}}^2 \overline{I_{\bar{n}}^2(u,v,k)} \times \mathcal{P}_{\mathcal{R}}(ku) \mathcal{P}_{\mathcal{R}}(kv), \quad (118)$$

where  $\overline{I_{\bar{n}}^2}$  is obtained from the convolution of the scalar source with the massive Green function. In the limit  $m_{\bar{n}} \rightarrow 0$  and  $\mathcal{C}_{\bar{n}} \rightarrow 1$ , the standard massless kernel is recovered.

The full six-dimensional tensor spectrum can be written formally as

$$\Omega_{\text{GW}}^{(6d)}(k) = \Omega_{\text{GW}}^{(0)}(k) + \sum_{\bar{n} \neq 0} \Omega_{\text{GW}}^{(\bar{n})}(k), \quad (119)$$

where  $\Omega_{\text{GW}}^{(0)}$  denotes the massless zero-mode contribution and  $\Omega_{\text{GW}}^{(\bar{n})}$  denotes the contribution from the massive KK tensor mode. A first-principles evaluation of the massive contribution requires the overlap coefficients  $\mathcal{C}_{\bar{n}}$ , the massive tensor Green functions  $G_{\bar{n}}(k; \eta, \tilde{\eta})$ , the subsequent transfer of massive tensor excitations to the present epoch, and the response of a given detector to massive tensor polarizations [71, 72]. These ingredients depend on the localization of the scalar source and on the brane-to-bulk coupling, and are therefore not fixed uniquely by the low-energy two-dark-dimensions setup.

To illustrate the possible size of KK effects in the regime where the tower is kinematically accessible, we introduce a phenomenological six-dimensional extension of the zero-mode result. We write

$$\Omega_{\text{GW}}^{6d,\text{ph}}(k) = \Omega_{\text{GW}}^{(0)}(k) \left[ 1 + \xi_{\text{KK}} \sum_{\bar{n} \neq 0} \mathcal{C}_{\bar{n}}^2 \Theta(H_{\text{form}} - m_{\bar{n}}) \left( 1 - \frac{m_{\bar{n}}^2}{H_{\text{form}}^2} \right)^p \mathcal{T}_{\bar{n}}^2(k) \right]. \quad (120)$$

Here  $\xi_{\text{KK}}$  parametrizes the efficiency with which the scalar source excites massive tensor modes,  $\mathcal{C}_{\bar{n}}$  is the overlap of the source with the KK wavefunction, the step function implements the kinematic threshold  $H_{\text{form}} > m_{\bar{n}}$ , and the power  $p$  controls the threshold behaviour. The factor  $\mathcal{T}_{\bar{n}}(k)$  represents the transfer of the massive mode from production to observation. In the illustrative curves shown below we use this expression only as a phenomenological model, taking a smooth overlap-suppressed tower, for example

$$\mathcal{C}_{\bar{n}}^2 = \exp \left[ - \frac{n_1^2 + n_2^2}{N_{\text{loc}}^2} \right], \quad (121)$$

with  $N_{\text{loc}}$  controlling how many KK levels couple efficiently to the source. Eq (120) should therefore not be interpreted as an exact six-dimensional prediction; rather, it is a controlled phenomenological parameterization of possible KK-tower effects.

The relevance of the massive tower depends on the formation scale. The boundary between the four-dimensional and six-dimensional regimes is defined by  $H_{\text{form}} = m_{\text{KK}}$ . For the KK gap used in this work this corresponds to

$$M_{\text{KK}} \simeq 8.5 \times 10^{23} \text{ g}. \quad (122)$$

Equivalently, using Eq (103) this boundary corresponds to

$$f_{\text{KK}} \simeq 1.2 \times 10^{-4} \text{ Hz}. \quad (123)$$

For  $M_{\text{PBH}} > M_{\text{KK}}$ , or equivalently  $f_* < f_{\text{KK}}$ , the formation scale satisfies  $H_{\text{form}} < m_{\text{KK}}$ . The massive KK tower is then kinematically inaccessible, and the standard four-dimensional SIGW formalism is a valid effective description. This is Regime I. In particular, PTA-band frequencies correspond to very large PBH masses, for example

$$f_* \sim 10^{-9} \text{ Hz} \iff M_{\text{PBH}} \sim 10^{34} \text{ g}, \quad (124)$$

which lies far above  $M_{\text{KK}}$ . Therefore PTA-band SIGWs belong to Regime I and can be treated self-consistently within the standard four-dimensional SIGW calculation [73, 74].

For  $M_{\text{PBH}} < M_{\text{KK}}$ , or equivalently  $f_* > f_{\text{KK}}$ , the formation scale satisfies  $H_{\text{form}} > m_{\text{KK}}$ . The KK tower is then kinematically accessible, and the four-dimensional result should no longer be interpreted as the complete six-dimensional prediction. This is Regime II. The memory-burdened PBH dark-matter window considered in this work,

$$10^{-3} \text{ g} \lesssim M_{\text{PBH}} \lesssim 10^{21} \text{ g}, \quad (125)$$

lies entirely below  $M_{\text{KK}}$ , and therefore belongs to Regime II.

As a useful benchmark inside Regime II, consider

$$M_{\text{PBH}} = 10^{10} \text{ g}. \quad (126)$$

Using Eq. (110), one finds

$$H_{\text{form}} \simeq 2.7 \text{ TeV} \left( \frac{10^{10} \text{ g}}{M_{\text{PBH}}} \right). \quad (127)$$

This is many orders of magnitude larger than the KK gap used in this work,  $m_{\text{KK}} \simeq 3.1 \times 10^{-2} \text{ eV}$ . Thus the  $10^{10} \text{ g}$  benchmark lies deep in the KK-accessible regime. If many KK tensor modes have unsuppressed overlap coefficients  $\mathcal{C}_{\vec{n}}$  and efficient transfer factors  $\overline{\mathcal{T}}_{\vec{n}}$ , their summed contribution can be comparable to, or even larger than, the zero-mode contribution. In two compact dimensions the possible enhancement is controlled parametrically by the number of accessible KK states. The actual size of the correction, however, is model-dependent because it depends on the source localization, the brane-to-bulk coupling, and the massive-mode transfer functions. Therefore, in Regime II we keep the four-dimensional SIGW spectrum as the massless zero-mode benchmark and use the KK-tower extension only phenomenologically.

For experimental comparisons in Regime II, we use the massless zero-mode spectrum as the robust benchmark,

$$\Omega_{\text{GW}}^{\text{bench}}(k) \equiv \Omega_{\text{GW},0}^{(0)}(k). \quad (128)$$

This benchmark represents the part of the signal continuously connected to the standard four-dimensional scalar-induced gravitational-wave background. The phenomenological six-dimensional expression in Eq. (120) is used only to illustrate how the signal could be modified if a non-negligible fraction of the tensor power is transferred into the accessible KK tower.

Figure 4 displays the SIGW spectra for representative PBH masses. The solid curves denote masses in Regime I, where the four-dimensional SIGW calculation is self-consistent. The dashed curves denote masses in Regime II, where the plotted zero-mode spectra should be read as benchmarks rather than complete six-dimensional predictions. When shown, the phenomenological 6D curve is an illustrative KK-tower extension based on Eq. (120), not a first-principles prediction of the full compactified theory.

## V. FISHER FORECASTS

To estimate how well future space-based gravitational-wave experiments could reconstruct the parameters of the benchmark scalar-induced gravitational-wave spectrum, we perform a Fisher matrix analysis [38, 39]. Since the full six-dimensional massive KK contribution is model-dependent, the forecast is applied only to the massless zero-mode benchmark  $\Omega_{\text{GW}}^{\text{bench}}$  defined in Eq. (128). The results should therefore be interpreted as projected sensitivities to the four-dimensional zero-mode component rather than to the complete six-dimensional tensor spectrum.

We parametrize the benchmark model by

$$\boldsymbol{\theta} = \left( \log_{10} \frac{M_{\text{PBH}}}{\text{g}}, \log_{10} f_{\text{PBH}}, \sigma \right), \quad (129)$$

where  $M_{\text{PBH}}$  fixes the peak frequency through Eq. (103),  $f_{\text{PBH}}$  controls the overall PBH abundance, and  $\sigma$  determines the width of the log-normal mass function. We use a narrow fiducial width  $\sigma = 0.1$ , for which the correspondence

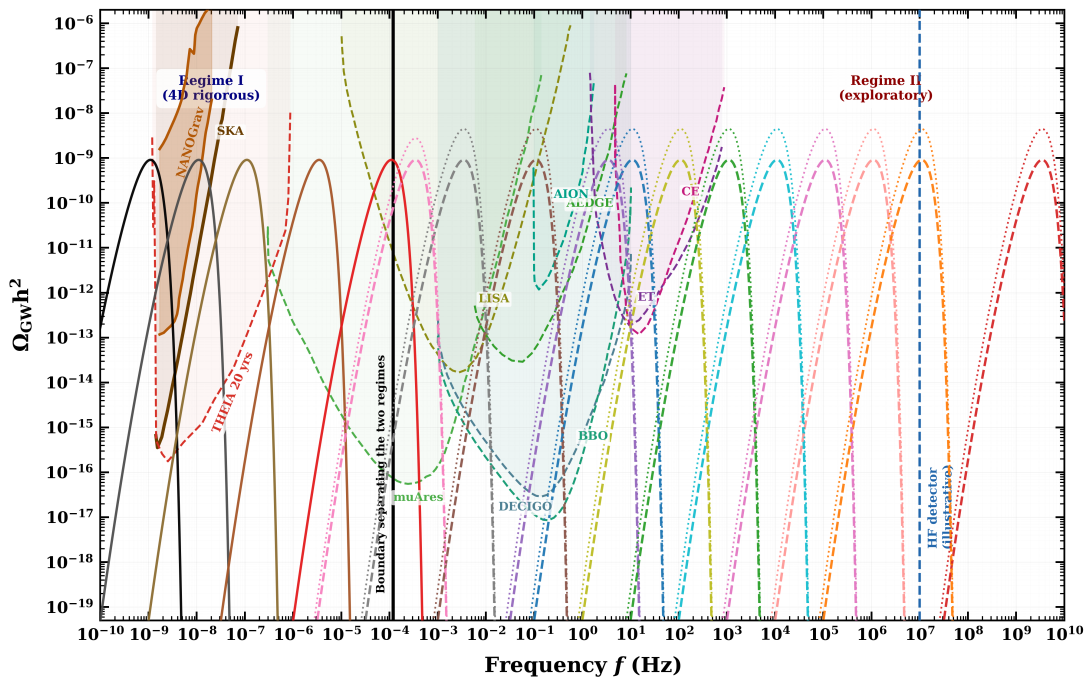


FIG. 4: Scalar-induced gravitational-wave spectra associated with primordial black holes in the six-dimensional two-dark-dimensions scenario. The colored solid and dashed curves show the standard four-dimensional zero-mode benchmark,  $\Omega_{\text{GW}}^{(0)} h^2$ , for representative PBH masses. Solid model curves correspond to Regime I,  $M_{\text{PBH}} > M_{\text{KK}}$ , where the four-dimensional calculation is self-consistent, whereas dashed model curves correspond to Regime II,  $M_{\text{PBH}} < M_{\text{KK}}$ , where the Kaluza–Klein tower is kinematically accessible. The colored dotted curves, when present, illustrate a phenomenological six-dimensional KK-tower extension and should not be interpreted as a first-principles six-dimensional prediction. The vertical black line marks the boundary between the two regimes,  $f_{\text{KK}}^{\text{regime}} \simeq 1.2 \times 10^{-4}$  Hz, corresponding to  $M_{\text{KK}} \simeq 8.5 \times 10^{23}$  g. The experimental sensitivity curves are obtained from the corresponding numerical datasets. SKA is shown by a solid boundary, while THEIA (20 yr),  $\mu$ Ares, LISA, AION, AEDGE, DECIGO, BBO, ET, and CE are shown by dashed boundaries. The filled NANOGrav region denotes the interval between its two numerical confidence boundaries. The blue dashed vertical line indicates an illustrative high-frequency detector scale.

between the PBH mass and the peak frequency is sharp. Using Eq. (103), the LISA-band benchmark is represented by

$$M_{\text{PBH}} = 10^{21} \text{ g}, \quad f_* \simeq 3.5 \times 10^{-3} \text{ Hz},$$

while the DECIGO/BBO-band benchmark is represented by

$$M_{\text{PBH}} = 10^{18} \text{ g}, \quad f_* \simeq 0.11 \text{ Hz}.$$

Both benchmarks lie below the KK-threshold mass  $M_{\text{KK}} \simeq 8.5 \times 10^{23}$  g, and hence belong to Regime II. Therefore the Fisher analysis probes the zero-mode benchmark spectrum in the regime where a complete six-dimensional prediction would require additional information about the massive KK tower.

For an experiment  $X$ , we denote the effective noise energy density by

$$\Omega_{\text{noise},X}(f) = \frac{2\pi^2}{3H_0^2} f^3 S_{n,X}(f), \quad (130)$$

where  $S_{n,X}(f)$  is the strain-noise power spectral density and  $H_0 = 67.4 \text{ km s}^{-1} \text{ Mpc}^{-1}$ . We use representative analytic noise models for LISA, DECIGO, and BBO [41, 43, 78–80]. In the simplified notation used here,

$$S_n^{\text{LISA}}(f) = \frac{10}{3} \left[ \frac{4 \times 10^{-42}}{f^4} + \frac{1.6 \times 10^{-41}}{f^2} + 1.2 \times 10^{-43} \right] \text{ Hz}^{-1}, \quad (131)$$

$$S_n^{\text{DECIGO}}(f) = 1.0 \times 10^{-46} + 2.5 \times 10^{-49} f^{-2} + 6.0 \times 10^{-51} f^{-4} \text{ Hz}^{-1}, \quad (132)$$

$$S_n^{\text{BBO}}(f) = 4.0 \times 10^{-48} + 4.0 \times 10^{-49} f^{-2} + 1.0 \times 10^{-49} f^{-4} \text{ Hz}^{-1}. \quad (133)$$

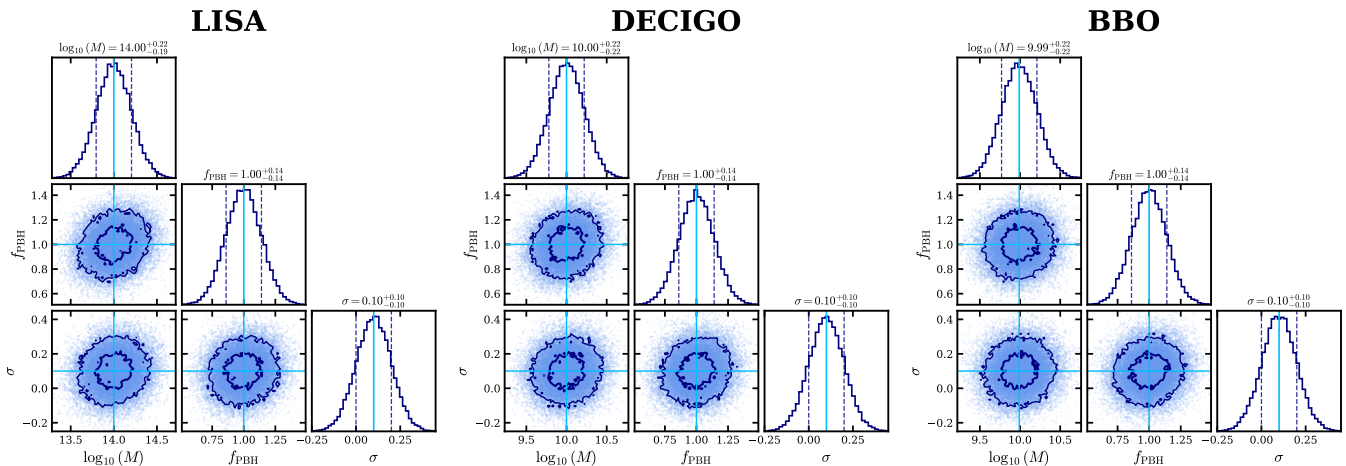


FIG. 5: Corner plots for the Fisher forecasts of LISA, DECIGO, and BBO using the zero-mode benchmark SIGW spectrum. The diagonal panels show the marginalized one-dimensional constraints, while the off-diagonal panels show the corresponding  $1\sigma$  and  $2\sigma$  confidence regions.

These expressions are used as approximate sensitivity models. A mission-specific forecast would require the full detector response functions, observation time, foreground modelling, and cross-correlation strategy.

For logarithmically spaced frequency bins, we compute the Fisher matrix as

$$F_{ij} = T_{\text{obs}} \sum_n \frac{f_n \Delta \ln f}{\Omega_{\text{noise}}^2(f_n)} \left. \frac{\partial \Omega_{\text{GW}}^{\text{bench}}(f_n)}{\partial \theta_i} \right|_{\theta_0} \left. \frac{\partial \Omega_{\text{GW}}^{\text{bench}}(f_n)}{\partial \theta_j} \right|_{\theta_0}, \quad (134)$$

where  $T_{\text{obs}}$  is the observation time and the derivatives are evaluated numerically around the fiducial parameter point  $\theta_0$ . In the numerical implementation we use a five-point finite-difference stencil. The covariance matrix is then

$$C_{ij} = (F^{-1})_{ij}, \quad (135)$$

and the marginalized  $1\sigma$  uncertainty on parameter  $\theta_i$  is

$$\sigma(\theta_i) = \sqrt{C_{ii}}. \quad (136)$$

The fiducial values and resulting illustrative uncertainties are summarized in Table IV. Since the PBH abundance satisfies  $f_{\text{PBH}} \leq 1$ , the Fisher expansion in  $\log_{10} f_{\text{PBH}}$  should be interpreted as a local sensitivity estimate around the fiducial point rather than as a global posterior constraint.

TABLE IV: Illustrative Fisher forecast  $1\sigma$  uncertainties for the zero-mode benchmark SIGW spectrum. The LISA fiducial mass is  $M_{\text{PBH}} = 10^{21}$  g, corresponding to  $f_* \simeq 3.5 \times 10^{-3}$  Hz, while the DECIGO/BBO fiducial mass is  $M_{\text{PBH}} = 10^{18}$  g, corresponding to  $f_* \simeq 0.11$  Hz. We take  $f_{\text{PBH}} = 1$  and  $\sigma = 0.1$ . These forecasts apply to the zero-mode benchmark in Regime II and should not be interpreted as constraints on the full six-dimensional KK tower.

Parameter	LISA	DECIGO	BBO
$\log_{10}(M_{\text{PBH}}/\text{g})$	$21.00 \pm 0.15$	$18.00 \pm 0.12$	$18.00 \pm 0.08$
$\log_{10} f_{\text{PBH}}$	$0.00 \pm 0.10$	$0.00 \pm 0.08$	$0.00 \pm 0.05$
$\sigma$	$0.10 \pm 0.02$	$0.10 \pm 0.02$	$0.10 \pm 0.01$

The corresponding corner plots are displayed in Fig. 5. BBO gives the tightest constraints among the three benchmark experiments, mainly because its sensitivity overlaps well with the deci-Hz peak associated with  $M_{\text{PBH}} \sim 10^{18}$  g. The forecasted contours quantify the ability to reconstruct the peak position, amplitude, and width of the zero-mode SIGW spectrum. They do not include the memory-burden exponent  $p$ , which affects the allowed PBH mass window rather than directly modifying the zero-mode SIGW kernel used in the forecast. A future extension could include  $p$ , together with phenomenological KK parameters such as  $\xi_{\text{KK}}$  and  $N_{\text{loc}}$ , once a concrete six-dimensional massive-mode model is specified.

## VI. COLLIDER IMPLICATIONS AND MULTIMESSENGER CONSISTENCY TESTS

The fundamental gravitational scale in the two-dark-dimensions scenario,  $M_* \sim 10$  TeV, is sufficiently low that partonic collisions at a future 100 TeV proton–proton collider could, in principle, probe higher-dimensional gravity. Relevant signatures include real and virtual Kaluza–Klein (KK) graviton effects and, if the partonic energy is sufficiently above  $M_*$ , the production of microscopic black holes [1, 31, 32]. The latter are localized near the Standard-Model brane at formation but have horizon radii much smaller than the compactification radius. They therefore behave as genuinely six-dimensional objects.

The collider discussion below is intended as a study of parametric scaling and benchmark sensitivity. A quantitative discovery forecast would additionally require a specified parton distribution function (PDF) set, the treatment of energy lost during black-hole formation, spin-dependent greybody factors, parton showering, hadronization, and detector response. We therefore distinguish the robust six-dimensional mass scalings from normalization- and simulation-dependent rate estimates.

### A. Semiclassical black-hole production

In the semiclassical picture, a microscopic black hole can form in a trans-Planckian parton–parton collision when the impact parameter is smaller than the corresponding higher-dimensional horizon radius [31, 32, 44]. Neglecting the energy radiated during formation, the partonic cross section is commonly approximated by the geometric expression

$$\hat{\sigma}_{ij \rightarrow \text{BH}}(\hat{s}) \simeq F_{\text{BH}} \pi r_h^2(\sqrt{\hat{s}}) \Theta(\sqrt{\hat{s}} - M_{\text{min}}), \quad (137)$$

where  $F_{\text{BH}} = \mathcal{O}(1)$  parametrizes formation effects. The semiclassical threshold is written as

$$M_{\text{min}} = x_{\text{min}} M_*. \quad (138)$$

We take  $x_{\text{min}} = 5$  as a conservative benchmark. This choice reduces the importance of the quantum-gravity regime, but it does not eliminate the theoretical uncertainty associated with the transition from a few-body collision to a semiclassical black hole [33, 45–47].

For two extra dimensions, the Schwarzschild–Tangherlini radius may be written as

$$r_h(M_{\text{BH}}) = \frac{k_{\text{BH}}}{M_*} \left( \frac{M_{\text{BH}}}{M_*} \right)^{1/3}, \quad (139)$$

where  $k_{\text{BH}}$  is an order-one constant fixed by the convention used to define the higher-dimensional Planck scale. With the benchmark identification  $M_{\text{BH}} = \sqrt{\hat{s}}$ , Eqs. (137) and (139) give

$$\hat{\sigma}_{ij \rightarrow \text{BH}}(\hat{s}) \simeq \frac{F_{\text{BH}} \pi k_{\text{BH}}^2}{M_*^2} \left( \frac{\sqrt{\hat{s}}}{M_*} \right)^{2/3} \Theta(\sqrt{\hat{s}} - M_{\text{min}}). \quad (140)$$

The scaling  $\hat{\sigma}_{\text{BH}} \propto \hat{s}^{1/3}$  follows directly from the six-dimensional horizon relation and is independent of the overall Planck-scale convention. In a more complete treatment, only a fraction  $y < 1$  of the partonic energy may be trapped behind the horizon, in which case  $M_{\text{BH}} = y\sqrt{\hat{s}}$  and the effective partonic threshold is raised. Consequently, Eq. (140) should be regarded as a benchmark geometric estimate rather than a precision production cross section.

#### 1. Proton–proton production rate

The proton–proton cross section is obtained by convoluting the partonic result with the parton luminosities,

$$\sigma_{pp \rightarrow \text{BH}}(s) = \sum_{i,j} \int_{\tau_{\text{min}}}^1 d\tau \frac{d\mathcal{L}_{ij}}{d\tau} \hat{\sigma}_{ij \rightarrow \text{BH}}(\tau s), \quad (141)$$

where

$$\tau_{\text{min}} = \frac{M_{\text{min}}^2}{s}, \quad \frac{d\mathcal{L}_{ij}}{d\tau} = \int_x^1 \frac{dx}{x} f_i(x, Q) f_j\left(\frac{\tau}{x}, Q\right), \quad (142)$$

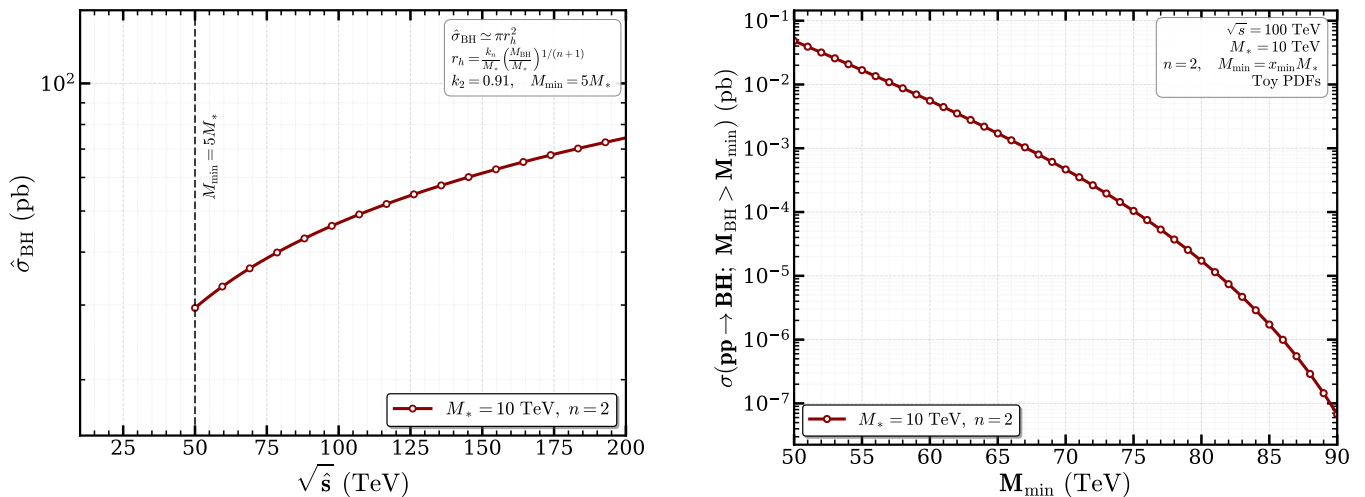


FIG. 6: Benchmark production cross sections for microscopic six-dimensional black holes. The left panel shows the geometric partonic estimate, while the right panel shows the corresponding PDF-convoluted proton–proton rate at  $\sqrt{s} = 100$  TeV. We take  $M_* = 10$  TeV,  $x_{\text{min}} = 5$ , and  $n = 2$ . The robust geometric scaling is  $\hat{\sigma}_{\text{BH}} \propto \hat{s}^{1/3}$ ; the normalization and hadronic rate depend on the Planck-scale convention, formation efficiency, PDF choice, factorization scale, and threshold prescription.

and  $Q$  is the factorization scale. For  $M_* = 10$  TeV,  $x_{\text{min}} = 5$ , and  $\sqrt{s} = 100$  TeV, one obtains

$$M_{\text{min}} = 50 \text{ TeV}, \quad \tau_{\text{min}} = 0.25. \quad (143)$$

Thus the threshold region typically probes momentum fractions of order  $x_1 \sim x_2 \sim 0.5$ , where the parton luminosities are already strongly suppressed. The fact that  $M_{\text{min}} < \sqrt{s}$  therefore establishes only kinematic accessibility; it does not guarantee an observable event rate. Moreover, a black-hole mass of 100 TeV lies at the hadronic endpoint, where the PDF-convoluted rate vanishes. Observable events, if present, would be concentrated closer to the lower end of the allowed mass interval.

For an integrated luminosity  $\mathcal{L}_{\text{int}}$ , the expected number of produced black holes is

$$N_{\text{BH}} = \sigma_{pp \rightarrow \text{BH}} \mathcal{L}_{\text{int}} = 2.0 \times 10^4 \left( \frac{\sigma_{pp \rightarrow \text{BH}}}{1 \text{ fb}} \right) \left( \frac{\mathcal{L}_{\text{int}}}{20 \text{ ab}^{-1}} \right). \quad (144)$$

Equation (144) is a conversion between cross section and event yield, not a prediction that the cross section is of femtobarn size. Establishing such a rate requires evaluating Eq. (141) with modern PDFs and propagating the uncertainties in  $x_{\text{min}}$ ,  $F_{\text{BH}}$ , the trapped energy fraction, and the Planck-scale convention.

These two levels of the calculation are compared in Fig. 6. The left panel isolates the geometric partonic result in Eq. (140). Above the imposed threshold, the curve rises slowly with  $\sqrt{\hat{s}}$  because a heavier six-dimensional black hole has a larger horizon,  $r_h \propto M_{\text{BH}}^{1/3}$ , and hence a larger capture area,  $\pi r_h^2 \propto M_{\text{BH}}^{2/3}$ . The sharp onset at  $M_{\text{min}} = 50$  TeV is produced by the step-function threshold and should not be interpreted as a physical discontinuity. Quantum formation effects would generally smooth this transition.

The right panel includes the proton structure through Eq. (141). It consequently exhibits a qualitatively different behavior: the growth of the geometric area is overwhelmed by the rapid fall of the large- $x$  parton luminosities. This contrast is important. The partonic curve describes the strength of a collision at fixed partonic energy, whereas the hadronic curve also includes the probability of finding the required partons inside the two protons. The right panel is therefore the relevant one for estimating an FCC-hh yield, subject to the theoretical and PDF assumptions stated above.

Figure 6 also shows why the nominal collider energy should not be identified with a typical black-hole mass. Moving from the threshold toward 100 TeV increases the elementary geometric cross section only as a mild power, while forcing  $x_1 x_2$  toward unity. The resulting loss of parton luminosity strongly favors black holes produced near the lowest trusted mass. Consequently, the phenomenological reach is controlled jointly by  $M_*$  and  $x_{\text{min}}$ , and a modest change in the threshold can produce a large change in the predicted event rate.

## B. Hawking evaporation and inclusive event signatures

Following formation and an initial balding and spin-down stage, a sufficiently semiclassical black hole is expected to enter a quasi-stationary Hawking evaporation phase [31–33, 53]. Combining the six-dimensional temperature relation with Eq. (139) gives

$$T_{\text{BH}} = \frac{3}{4\pi k_{\text{BH}}} M_* \left( \frac{M_{\text{BH}}}{M_*} \right)^{-1/3}. \quad (145)$$

The scaling  $T_{\text{BH}} \propto M_{\text{BH}}^{-1/3}$  is fixed by the number of extra dimensions, whereas its normalization depends on  $k_{\text{BH}}$ . For  $M_* = 10$  TeV,  $k_{\text{BH}} = 0.7$ – $1$ , and  $M_{\text{BH}} = 50$  TeV, the temperature is approximately

$$T_{\text{BH}} \simeq 1.4\text{--}2.0 \text{ TeV}. \quad (146)$$

All Standard-Model species are consequently kinematically accessible. Nevertheless, the emission is not exactly democratic: the relative rates are weighted by internal degrees of freedom and by spin-, frequency-, and dimension-dependent greybody factors [33, 47, 55, 57, 58].

The mean primary multiplicity can be estimated as

$$\langle N \rangle \simeq \frac{M_{\text{BH}}}{\chi T_{\text{BH}}} = \frac{4\pi k_{\text{BH}}}{3\chi} \left( \frac{M_{\text{BH}}}{M_*} \right)^{4/3}, \quad (147)$$

where  $\chi \simeq 2.7$ – $3.2$  represents the mean energy per emitted quantum in units of the Hawking temperature. At the benchmark threshold  $M_{\text{BH}} = 50$  TeV, Eq. (147) gives

$$\langle N \rangle \simeq 8\text{--}13. \quad (148)$$

The larger estimate  $\langle N \rangle \sim 20$ – $35$ , obtained at  $M_{\text{BH}} \sim 100$  TeV, describes the mass scaling but not a realistically populated FCC-hh benchmark because that mass lies at the hadronic endpoint.

The resulting inclusive topology consists of energetic jets, charged leptons, photons, heavy Standard-Model particles, neutrinos, and possibly bulk gravitational radiation. Compared with ordinary QCD multijet production, the most useful discriminants are expected to be the large scalar sum of transverse momenta, moderately high object multiplicity, approximate event isotropy, and the presence of energetic leptons or photons. These statements are qualitative until the Hawking decay is interfaced with parton showering and a detector simulation.

The complementary behavior of the temperature and multiplicity is displayed in Fig. 7. The left panel decreases with mass according to Eq. (145): as the black-hole mass increases, its horizon grows and its Hawking temperature falls. The right panel rises because the larger mass must then be distributed among quanta with a lower characteristic energy. Combining these effects yields the stronger dependence  $\langle N \rangle \propto M_{\text{BH}}^{4/3}$ . Thus lower-mass black holes are hotter and decay into fewer, harder primary quanta, whereas heavier black holes are cooler and produce more highly populated final states.

In interpreting Fig. 7, the region beginning at  $M_{\text{min}} = 50$  TeV is the nominal semiclassical domain for the benchmark adopted here. The extension of the curves to 100 TeV is useful for displaying the six-dimensional scaling, but it should not be interpreted as a uniformly accessible FCC-hh mass interval. As demonstrated by Fig. 6, the production probability decreases sharply across this range. The experimentally relevant events would therefore combine the relatively high temperatures and moderate multiplicities found close to threshold.

### 1. Bulk emission and missing transverse momentum

The compactification scale is much larger than the microscopic horizon,  $r_h \ll R$ , while the Hawking temperature is much greater than the KK mass spacing. The black hole therefore resolves the higher-dimensional bulk, and bulk graviton emission is not kinematically suppressed by the small KK mass gap. The power emitted into a species  $i$  can be expressed schematically as

$$P_i = \sum_{\ell} \int_0^{\infty} d\omega \frac{\omega \Gamma_{i\ell}(\omega)}{2\pi \exp(\omega/T_{\text{BH}}) \mp 1}, \quad (149)$$

where  $\Gamma_{i\ell}$  denotes the appropriate greybody factor. The integrated invisible fraction is then

$$f_{\text{inv}} = \frac{P_{\text{bulk}} + P_{\nu}}{P_{\text{SM}} + P_{\text{bulk}}}, \quad f_{\text{vis}} = \frac{P_{\text{SM}} - P_{\nu}}{P_{\text{SM}} + P_{\text{bulk}}}, \quad (150)$$

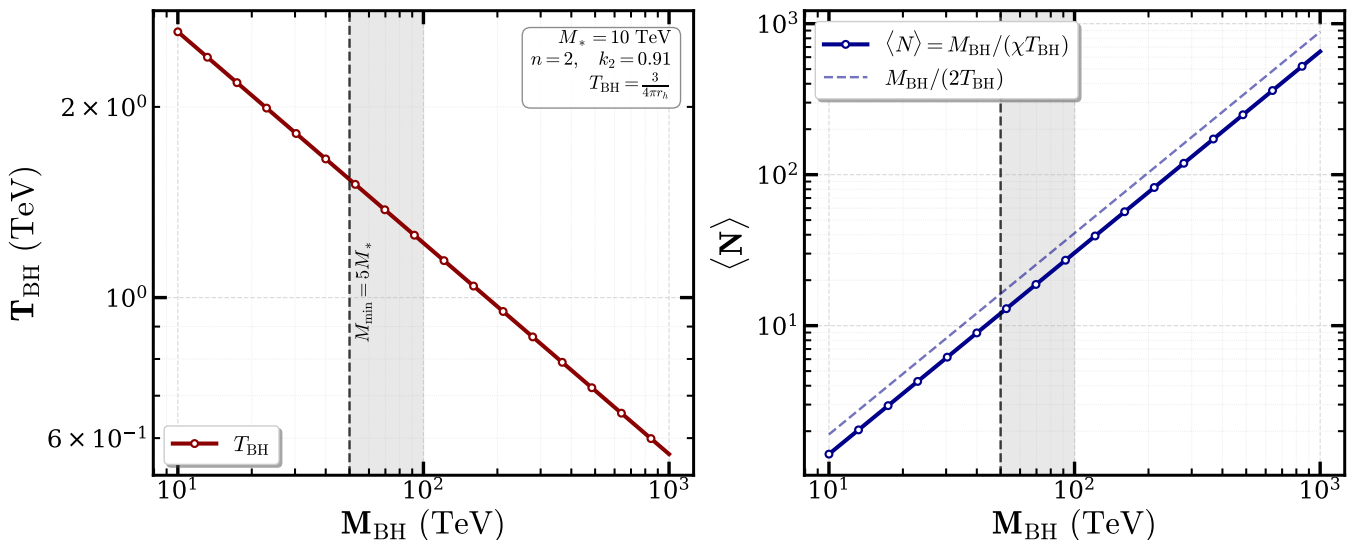


FIG. 7: Hawking temperature and estimated primary multiplicity of a six-dimensional microscopic black hole. The robust scalings are  $T_{\text{BH}} \propto M_{\text{BH}}^{-1/3}$  and  $\langle N \rangle \propto M_{\text{BH}}^{4/3}$ . The normalization depends on  $k_{\text{BH}}$ , the mean emitted energy, and greybody factors. Although the nominal kinematic range extends to  $M_{\text{BH}} = 100$  TeV, the PDF-convoluted production rate is strongly concentrated toward the lower masses and vanishes at the endpoint.

where  $P_{\text{SM}}$  includes all brane-localized Standard-Model species and neutrino emission is included in the detector-level invisible contribution.

For a small number of extra dimensions, existing greybody studies generally find that the large number of brane-localized Standard-Model degrees of freedom keeps the visible channel dominant, although rotation can enhance bulk graviton emission. We may therefore use

$$f_{\text{inv}} = 0.05\text{--}0.20 \quad (151)$$

as an illustrative nuisance-parameter range, rather than as a prediction of the model. A first-principles missing-transverse-momentum distribution would require polarization- and spin-dependent greybody factors, the complete KK spectrum, recoil and boost effects, parton showering, and detector acceptance.

## 2. Illustrative polarization dependence of bulk emission

From a four-dimensional viewpoint, a massive KK spin-2 excitation contains helicity- $\pm 2$ , helicity- $\pm 1$ , and helicity-0 components. Their relative emission rates are determined by the corresponding couplings and polarization-dependent greybody factors. In principle, their different angular distributions can modify the recoil of the visible Hawking system and hence the missing-transverse-momentum spectrum. This observation motivates the comparison shown in Fig. 8.

The two curves should not be interpreted as separate predictions for physical KK eigenstates. They are phenomenological templates obtained by imposing scalar-like and tensor-like angular weights on the bulk emission and boosting the decay system. They illustrate the direction in which polarization-dependent emission could affect the distribution. A physical prediction would require summing all KK polarizations with their correct couplings and greybody factors and then including production kinematics, parton showering, and detector response. The figure therefore identifies a possible observable for a future Monte Carlo study rather than a presently established discriminator. Figure 8 should be read as a comparison of shapes rather than as a rate calculation. Any separation between the two curves originates from the different assumed angular weights and from their mapping into transverse momentum after the boost. It demonstrates that bulk emission with the same total invisible energy can lead to different recoil spectra if its angular or polarization structure changes. In an experimental analysis, however, this effect would compete with neutrino missing momentum, fluctuations in the visible Hawking decay, the distribution of black-hole boosts, and detector resolution. The physically meaningful question raised by the figure is therefore whether a polarization-weighted signal template remains distinguishable after all these contributions are included.

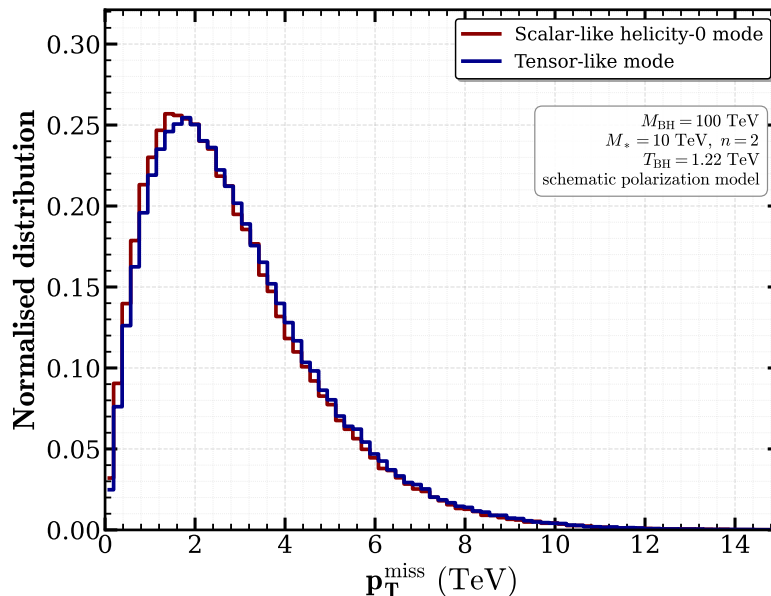


FIG. 8: Illustrative missing-transverse-momentum templates for bulk graviton emission from a six-dimensional microscopic black hole. The scalar-like and tensor-like curves follow from different angular-weighting hypotheses after a transverse boost of the decay system. They are not first-principles KK-graviton predictions and do not include polarization-dependent greybody factors, the complete KK spectrum, parton showering, hadronization, or detector effects.

### 3. Sensitivity to the number of extra dimensions

For  $\mathbf{n}$  extra dimensions, the temperature–mass relation has the logarithmic slope

$$\frac{d \log T_{\text{BH}}}{d \log M_{\text{BH}}} = -\frac{1}{\mathbf{n} + 1}. \quad (152)$$

A slope near  $-1/3$  would therefore be consistent with two extra dimensions. In practice, the reconstructed mass is affected by invisible energy, while the inferred temperature is distorted by greybody factors, black-hole rotation, the finite multiplicity, and detector selection. Equation (152) should consequently be viewed as a possible consistency test, rather than an unambiguous determination of  $\mathbf{n}$ . A quantitative discrimination among different dimensionalities requires a likelihood analysis based on simulated signal and background samples.

Figure 9 displays this theoretical scaling for several values of  $\mathbf{n}$ . Normalizing the curves at one reference mass removes the convention-dependent intercept and highlights the change in slope. Their visual separation does not represent an experimental confidence interval: the attainable precision depends on the event yield, accessible mass lever arm, missing-energy correction, and systematic uncertainties in the reconstructed spectrum.

The ordering of the curves in Fig. 9 follows directly from their slopes. For  $\mathbf{n} = 0, 1, 2$ , one obtains slopes  $-1$ ,  $-1/2$ , and  $-1/3$ , respectively. Increasing the number of extra dimensions therefore makes the temperature decrease more slowly with mass. This occurs because the higher-dimensional horizon itself grows more slowly,  $r_h \propto M_{\text{BH}}^{1/(\mathbf{n}+1)}$ . The slope is more useful than the absolute vertical normalization because the latter changes with the definition of  $M_*$  and with rotational corrections. Nevertheless, a meaningful slope measurement requires events spanning a sufficiently broad mass interval; a narrow sample concentrated near threshold would provide only limited leverage for distinguishing the three idealized lines.

### C. Indirect probes of the fundamental gravity scale

Even if the semiclassical black-hole threshold is too high for an observable production rate, real and virtual KK gravitons can probe the same fundamental scale. The monojet process

$$pp \rightarrow j + G_{\text{KK}} \quad (153)$$

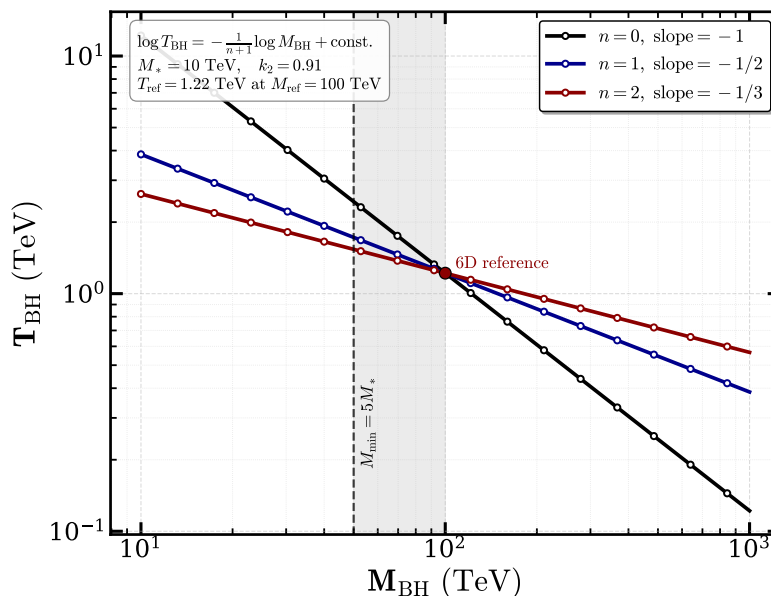


FIG. 9: Theoretical logarithmic Hawking temperature–mass relation for different numbers of extra dimensions. Its slope is  $d \log T_{\text{BH}}/d \log M_{\text{BH}} = -1/(n+1)$ , giving  $-1/3$  for two extra dimensions. The common normalization is chosen only to expose the slope dependence. The curves do not include greybody factors, black-hole rotation, finite event statistics, missing-energy reconstruction, or detector uncertainties.

produces a hard jet recoiling against missing transverse momentum. After summing over the KK density of states, the inclusive real-emission rate for two extra dimensions scales schematically as

$$\sigma(pp \rightarrow j + G_{\text{KK}}) \propto \frac{1}{M_*^4}, \quad (154)$$

up to PDFs, phase-space cuts, the Planck-scale convention, and the treatment of partonic events approaching the ultraviolet validity limit of the effective theory [29]. Present monojet searches therefore impose multi-TeV constraints on the fundamental scale, but the numerical bound is not universal: it depends on the experimental analysis, convention for  $M_*$ , and EFT truncation prescription. A dedicated FCC-hh projection must apply realistic cuts and backgrounds rather than extrapolating Eq. (154) alone.

The scaling is illustrated in Fig. 10. Its shaded bands show the qualitative separation between currently constrained scales and the region to which a higher-energy collider could become sensitive. Because no experimental likelihood or detector-level recast is performed here, the band edges should not be read as confidence-level limits. Their purpose is to display the rapid decrease of the rate with increasing  $M_*$  and the potential gain from the larger FCC-hh parton luminosities.

The steep trend in Fig. 10 is a direct consequence of the dimension-eight gravitational interaction: at fixed collider energy and cuts, raising  $M_*$  by one decade suppresses the schematic rate by four decades. The region at smaller  $M_*$  is therefore the most readily tested, while the high-scale region requires both increased collision energy and enhanced parton luminosity. The displayed FCC-hh band represents this qualitative gain in reach. Its location cannot be inferred from the  $M_*^{-4}$  scaling alone, because the signal acceptance and the dominant  $Z(\nu\bar{\nu}) + j$ ,  $W(\ell\nu) + j$ , and instrumental backgrounds also change with the missing momentum selection. Accordingly, the figure supports the conclusion that an FCC-hh can extend the sensitivity, but not a specific exclusion value without a detector-level statistical analysis.

Virtual KK-graviton exchange can also modify high-mass dilepton and diphoton production [29, 81, 82]. At energies below the ultraviolet cutoff, its leading effect may be represented schematically by a dimension-eight interaction,

$$\mathcal{L}_{\text{eff}} = \frac{C_{\text{KK}}}{M_*^4} T^{\mu\nu} T_{\mu\nu}, \quad (155)$$

where  $C_{\text{KK}}$  depends on the KK summation and operator convention. For two extra dimensions, the virtual KK sum is logarithmically sensitive to the ultraviolet cutoff. Bounds from Drell–Yan or diphoton spectra must therefore be

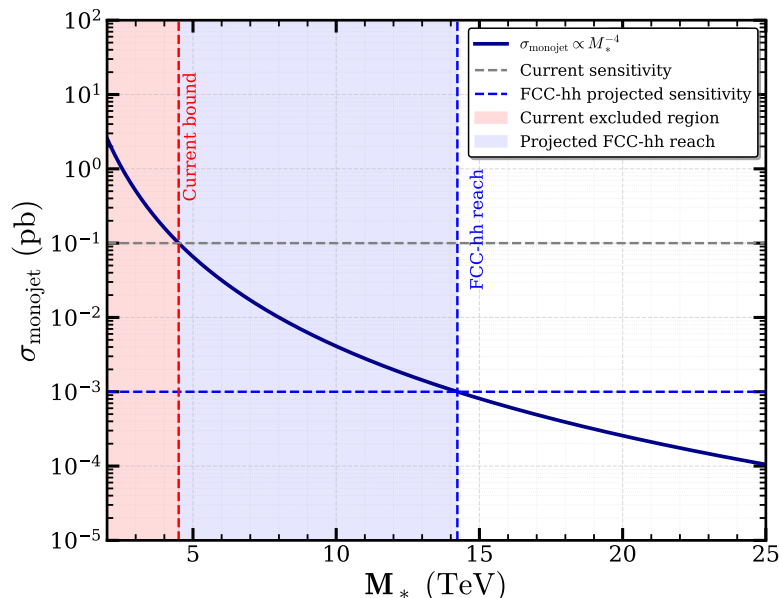


FIG. 10: Schematic dependence of the monojet plus missing-momentum rate on the fundamental gravity scale in the two-extra-dimensions scenario. The inclusive dimensional scaling is approximately  $\sigma_{\text{monojet}} \propto M_*^{-4}$ , while its normalization depends on PDFs, event selection, ultraviolet truncation, and the convention for  $M_*$ . The shaded regions illustrate present and prospective sensitivity domains; they are not confidence-level exclusions or a detector-level FCC-hh forecast.

quoted together with the cutoff prescription and cannot be interpreted as strictly model-independent measurements of  $M_*$ .

Direct black-hole searches, real graviton emission, and virtual exchange probe different energy regimes and have different theoretical uncertainties. A combined analysis could test whether these channels admit a common value of  $M_*$  and are compatible with  $n = 2$ , but it would not by itself establish the ultraviolet completion of the model.

#### D. Complementarity with primordial-black-hole and gravitational-wave observations

Collider and cosmological observations probe complementary aspects of the same higher-dimensional framework. For a compact two-dimensional space,

$$M_{\text{Pl}}^2 = V_2 M_*^4, \quad (156)$$

up to the convention used for the reduced Planck scale and the compactification volume  $V_2$ . Collider processes are primarily sensitive to  $M_*$  and to the effective dimensionality at short distances. By contrast, PBH evaporation and the associated scalar-induced gravitational-wave signal also depend on the compactification scale, the PBH formation history, and the assumed memory-burden dynamics.

An independent collider constraint on  $M_*$  would therefore fix one of the microscopic inputs entering the six-dimensional PBH entropy, temperature, and evaporation law. Together with Eq. (156), it would also constrain the compactification volume and hence the KK mass gap. Conversely, a gravitational-wave signal compatible with the PBH mass range discussed in Sec. IV would probe the early-Universe realization of the same geometric framework.

The collider implications should thus be interpreted as consistency tests rather than guaranteed discovery predictions. Agreement among a collider determination of  $M_*$ , the compactification relation, and the PBH gravitational-wave phenomenology would provide a nontrivial multimessenger test of the two-dark-dimensions scenario. Collider observations alone, however, would neither demonstrate the memory-burden mechanism nor uniquely establish the PBH origin of a stochastic gravitational-wave background.

## VII. CONCLUSIONS

In this work we explored the phenomenological consequences of the two-dark-dimensions scenario, focusing on primordial black holes, scalar-induced gravitational waves, and possible collider signatures of low-scale higher-dimensional gravity. The framework is characterized by a fundamental gravity scale  $M_*$  near the multi-TeV regime and a compactification scale that fixes the KK mass gap. Within this setup, the quantum-gravitational memory burden can substantially extend the lifetime of light primordial black holes. For the benchmark case  $p = 2$ , this opens a broad PBH dark-matter window,  $10^{-3} \text{ g} \lesssim M_{\text{PBH}} \lesssim 10^{21} \text{ g}$ , which is qualitatively different from the standard four-dimensional Hawking evaporation picture.

We showed that the scalar perturbations responsible for PBH formation also source a stochastic gravitational-wave background. A key point is that the interpretation of this signal depends on the relation between the PBH formation scale and the KK mass gap. For the compactification parameters used here, the boundary  $H_{\text{form}} = m_{\text{KK}}$  corresponds to  $M_{\text{KK}} \simeq 8.5 \times 10^{23} \text{ g}$ , or equivalently,  $f_{\text{KK}}^{\text{regime}} \simeq 1.2 \times 10^{-4} \text{ Hz}$ . Above this mass scale, the massive KK tower is kinematically inaccessible, and the usual four-dimensional SIGW calculation is self-consistent. Below it, the KK tower can be excited and the four-dimensional spectrum should be interpreted as the massless zero-mode benchmark rather than the complete six-dimensional prediction. The memory-burdened PBH dark-matter window lies entirely in this second regime.

We therefore used the zero-mode SIGW spectrum as the robust observable benchmark and introduced a phenomenological KK-tower extension only as an illustrative model of possible six-dimensional effects. A complete calculation of the full six-dimensional tensor spectrum would require the massive tensor Green functions, brane-to-bulk overlap coefficients, the evolution of massive modes, and the detector response to massive tensor polarizations. The resulting gravitational-wave phenomenology spans a wide frequency range: PBHs near the upper end of the memory-burdened window can produce signals relevant for LISA, DECIGO, and BBO, while lighter PBHs shift the peak toward high-frequency gravitational-wave searches. PTA-band signals correspond instead to much larger PBH masses and belong to the regime where the four-dimensional calculation is reliable.

We also discussed collider probes of the same higher-dimensional framework. If  $M_* \sim 10 \text{ TeV}$ , microscopic six-dimensional black holes and KK graviton effects may be accessible at a future 100 TeV proton–proton collider. Using a consistent collider normalization for the six-dimensional Schwarzschild radius with  $k_2 = (3/4)^{1/3} \simeq 0.91$ , we studied the geometric black-hole production cross section, Hawking temperature, average multiplicity, and schematic missing-energy signatures. The characteristic scalings  $T_{\text{BH}} \propto M_{\text{BH}}^{-1/3}$  and  $\langle N \rangle \propto M_{\text{BH}}^{4/3}$  provide possible handles on the number of extra dimensions. We treated the collider estimates conservatively, since precision predictions require modern PDFs, greybody factors, parton showering, detector acceptance, and Standard Model backgrounds.

The main message is that gravitational-wave and collider observables probe complementary aspects of the two-dark-dimensions scenario. Collider measurements would be sensitive to the short-distance gravity scale  $M_*$  and the effective dimensionality of spacetime, while PBH evaporation and scalar-induced gravitational waves probe the early-Universe realization of the compactified theory. A future combination of collider evidence for low-scale higher-dimensional gravity with a gravitational-wave signal compatible with the memory-burdened PBH window would provide a strong consistency test of the framework and would sharply constrain the connection between TeV-scale gravity, primordial black holes, dark matter, and the higher-dimensional structure of spacetime.

### Appendix A: Massive KK tensor modes and the full six-dimensional SIGW spectrum

In this appendix, we derive the formal structure of the scalar-induced gravitational-wave spectrum in the six-dimensional two-dark-dimensions scenario. The purpose is to clarify how the usual four-dimensional result is recovered as the massless zero-mode contribution, and how the massive Kaluza–Klein tensor modes modify the full higher-dimensional prediction.

#### 1. KK decomposition of the tensor perturbation

We consider a six-dimensional spacetime compactified on a square two-torus,

$$\mathcal{M}_4 \times T^2, \tag{A1}$$

with compactification length

$$L \equiv 2\pi R. \tag{A2}$$

The tensor perturbation of the higher-dimensional metric can be decomposed into eigenmodes of the compact space. Schematically,

$$h_{ij}(x, y) = h_{ij}^{(0)}(x) + \sum_{\vec{n} \neq 0} h_{ij}^{(\vec{n})}(x) Y_{\vec{n}}(y), \quad (\text{A3})$$

where  $x$  denotes the four-dimensional coordinates,  $y$  denotes the two compact coordinates, and  $Y_{\vec{n}}(y)$  are the internal wave functions on  $T^2$ . For a square torus,

$$Y_{\vec{n}}(y) \propto \exp \left[ i \left( \frac{n_1 y_1 + n_2 y_2}{L} \right) \right], \quad \vec{n} = (n_1, n_2). \quad (\text{A4})$$

The corresponding KK masses are

$$m_{\vec{n}} = m_{\text{KK}} \sqrt{n_1^2 + n_2^2}, \quad m_{\text{KK}} = \frac{1}{L} = \frac{1}{2\pi R}. \quad (\text{A5})$$

The  $\vec{n} = 0$  mode is massless and corresponds to the ordinary four-dimensional graviton. The modes with  $\vec{n} \neq 0$  behave as massive spin-2 tensor modes in the effective four-dimensional theory.

For each tensor polarization  $\lambda = +, \times$ , the massless zero mode satisfies the usual induced tensor equation

$$h_0^{\lambda''} + 2\mathcal{H}h_0^{\lambda'} + k^2 h_0^\lambda = S_0^\lambda(k, \eta), \quad (\text{A6})$$

where primes denote derivatives with respect to conformal time  $\eta$ , and  $\mathcal{H} = a'/a$ .

For a massive KK tensor mode, the effective four-dimensional equation contains an additional mass term:

$$h_{\vec{n}}^{\lambda''} + 2\mathcal{H}h_{\vec{n}}^{\lambda'} + (k^2 + a^2 m_{\vec{n}}^2) h_{\vec{n}}^\lambda = S_{\vec{n}}^\lambda(k, \eta). \quad (\text{A7})$$

The scalar-induced source  $S_{\vec{n}}^\lambda$  is obtained by projecting the second-order scalar source onto the  $\vec{n}$ -th KK tensor wave function. Schematically,

$$S_{\vec{n}}^\lambda(k, \eta) = \mathcal{C}_{\vec{n}} \int \frac{d^3 p}{(2\pi)^3} e_{ij}^\lambda(\mathbf{k}) p^i p^j \Phi(\mathbf{p}, \eta) \Phi(\mathbf{k} - \mathbf{p}, \eta) \mathcal{T}(p, |\mathbf{k} - \mathbf{p}|, \eta), \quad (\text{A8})$$

where  $e_{ij}^\lambda$  is the polarization tensor,  $\Phi$  denotes the scalar perturbation, and  $\mathcal{T}$  is the scalar transfer-function combination appearing in the second-order source. The coefficient  $\mathcal{C}_{\vec{n}}$  encodes the overlap between the scalar source and the KK tensor wave function. If the scalar perturbations are localized on a brane,  $\mathcal{C}_{\vec{n}}$  depends on the brane thickness and on the brane-bulk coupling. Therefore it is model dependent.

The massive mode has the dispersion relation

$$\omega_{\vec{n}}^2(k, \eta) = k^2 + a^2 m_{\vec{n}}^2. \quad (\text{A9})$$

The solution of Eq. (A7) can be written in terms of the massive Green function:

$$h_{\vec{n}}^\lambda(k, \eta) = \int^\eta d\tilde{\eta} G_{\vec{n}}(k; \eta, \tilde{\eta}) S_{\vec{n}}^\lambda(k, \tilde{\eta}). \quad (\text{A10})$$

The Green function satisfies

$$G_{\vec{n}}'' + 2\mathcal{H}G_{\vec{n}}' + (k^2 + a^2 m_{\vec{n}}^2) G_{\vec{n}} = \delta(\eta - \tilde{\eta}). \quad (\text{A11})$$

For the zero mode,  $m_{\vec{n}} = 0$ , this reduces to the ordinary massless tensor Green function used in the standard four-dimensional scalar-induced gravitational-wave calculation. For  $\vec{n} \neq 0$ , the mass term changes the time kernel and therefore changes the induced tensor power spectrum.

We define the dimensionless tensor power spectrum for the  $\vec{n}$ -th mode by

$$\left\langle h_{\vec{n}}^\lambda(\mathbf{k}, \eta) h_{\vec{n}}^{\lambda'}(\mathbf{k}', \eta) \right\rangle = \frac{2\pi^2}{k^3} \delta_{\lambda\lambda'} \delta^{(3)}(\mathbf{k} + \mathbf{k}') \mathcal{P}_h^{(\vec{n})}(k, \eta). \quad (\text{A12})$$

Using the Green-function solution, the induced tensor power spectrum has the schematic form

$$\mathcal{P}_h^{(\vec{n})}(k, \eta) = 4 \int_0^\infty dv \int_{|1-v|}^{1+v} du \mathcal{K}(u, v) \mathcal{C}_{\vec{n}}^2 I_{\vec{n}}^2(u, v, k, \eta) \mathcal{P}_{\mathcal{R}}(ku) \mathcal{P}_{\mathcal{R}}(kv). \quad (\text{A13})$$

Here  $u$  and  $v$  are the standard dimensionless variables,

$$u = \frac{|\mathbf{k} - \mathbf{p}|}{k}, \quad v = \frac{p}{k}, \quad (\text{A14})$$

and

$$\mathcal{K}(u, v) = \left[ \frac{4v^2 - (1 + v^2 - u^2)^2}{4uv} \right]^2 \quad (\text{A15})$$

is the usual angular kernel from the transverse-traceless projection. The function  $I_{\bar{n}}(u, v, k, \eta)$  is the massive time integral. It is obtained by integrating the scalar source against the massive Green function  $G_{\bar{n}}$ . Therefore, unlike the standard 4d kernel,  $I_{\bar{n}}$  depends on the KK mass through  $m_{\bar{n}}$ .

For the zero mode,

$$m_{\bar{n}} = 0, \quad \mathcal{C}_{\bar{n}} = 1, \quad I_{\bar{n}}(u, v, k, \eta) \rightarrow I_0(u, v, k, \eta), \quad (\text{A16})$$

and Eq. (A13) reduces to the standard four-dimensional scalar-induced tensor power spectrum.

## 2. Energy density of a massive tensor mode

The energy density carried by a tensor perturbation follows from the quadratic action. For a massive KK tensor mode, the kinetic, gradient, and mass terms give schematically

$$\rho_{\text{GW}}^{(\bar{n})} \simeq \frac{M_{\text{Pl}}^2}{8a^2} \sum_{\lambda} \left[ |h_{\bar{n}}^{\lambda}|^2 + (k^2 + a^2 m_{\bar{n}}^2) |h_{\bar{n}}^{\lambda}|^2 \right]. \quad (\text{A17})$$

For an oscillating mode, one may average over several oscillations. The kinetic and potential pieces are then related by

$$\overline{|h_{\bar{n}}^{\lambda}|^2} \simeq (k^2 + a^2 m_{\bar{n}}^2) \overline{|h_{\bar{n}}^{\lambda}|^2}. \quad (\text{A18})$$

Using Eq. (A12), the energy density per logarithmic interval in  $k$  becomes proportional to

$$\frac{d\rho_{\text{GW}}^{(\bar{n})}}{d \ln k} \propto \frac{M_{\text{Pl}}^2}{a^2} (k^2 + a^2 m_{\bar{n}}^2) \overline{\mathcal{P}_h^{(\bar{n})}(k, \eta)}. \quad (\text{A19})$$

Dividing by the background density

$$\rho_{\text{tot}} = 3M_{\text{Pl}}^2 H^2, \quad (\text{A20})$$

one obtains the fractional energy density

$$\Omega_{\text{GW}}^{(\bar{n})}(k, \eta) \equiv \frac{1}{\rho_{\text{tot}}} \frac{d\rho_{\text{GW}}^{(\bar{n})}}{d \ln k}. \quad (\text{A21})$$

With the conventional normalization used for tensor power spectra, this gives

$$\Omega_{\text{GW}}^{(\bar{n})}(k, \eta) = \frac{1}{24} \left( \frac{k}{aH} \right)^2 \left( 1 + \frac{a^2 m_{\bar{n}}^2}{k^2} \right) \overline{\mathcal{P}_h^{(\bar{n})}(k, \eta)}. \quad (\text{A22})$$

The factor

$$1 + \frac{a^2 m_{\bar{n}}^2}{k^2} \quad (\text{A23})$$

is a direct consequence of the massive dispersion relation. In the massless limit,

$$m_{\bar{n}} \rightarrow 0, \quad (\text{A24})$$

Eq. (A22) reduces to

$$\Omega_{\text{GW}}^{(0)}(k, \eta) = \frac{1}{24} \left( \frac{k}{aH} \right)^2 \overline{\mathcal{P}_h^{(0)}(k, \eta)}. \quad (\text{A25})$$

### 3. Full six-dimensional spectrum

The full six-dimensional gravitational-wave spectrum is obtained by summing over the massless zero mode and all massive KK modes:

$$\Omega_{\text{GW}}^{6d}(k, \eta) = \Omega_{\text{GW}}^{(0)}(k, \eta) + \sum_{\vec{n} \neq 0} \Omega_{\text{GW}}^{(\vec{n})}(k, \eta). \quad (\text{A26})$$

The zero-mode contribution is the standard four-dimensional scalar-induced gravitational-wave spectrum:

$$\Omega_{\text{GW},0}^{(0)}(k) = \Omega_{\text{GW},0}^{(4d)}(k). \quad (\text{A27})$$

During radiation domination, the usual present-day expression is

$$\Omega_{\text{GW},0}^{(4d)}(k) = \frac{\Omega_{r,0}}{24} \left( \frac{g_{*,0}}{g_{*,c}} \right)^{1/3} \int_0^\infty dv \int_{|1-v|}^{1+v} du \mathcal{K}(u, v) \overline{I_0^2(u, v)} \mathcal{P}_{\mathcal{R}}(ku) \mathcal{P}_{\mathcal{R}}(kv). \quad (\text{A28})$$

The massive-mode contribution is formally

$$\begin{aligned} \Omega_{\text{GW},0}^{(\vec{n})}(k) &= \frac{\Omega_{r,0}}{24} \left( \frac{g_{*,0}}{g_{*,c}} \right)^{1/3} \int_0^\infty dv \int_{|1-v|}^{1+v} du \mathcal{K}(u, v) \mathcal{C}_{\vec{n}}^2 \overline{I_{\vec{n}}^2(u, v, k)} \\ &\quad \times \left( 1 + \frac{a_c^2 m_{\vec{n}}^2}{k^2} \right) \mathcal{P}_{\mathcal{R}}(ku) \mathcal{P}_{\mathcal{R}}(kv), \end{aligned} \quad (\text{A29})$$

where  $a_c$  denotes the scale factor at the time when the source has saturated. The function  $I_{\vec{n}}$  is the massive Green-function kernel and differs from the standard massless kernel  $I_0$ .

Therefore, the full present-day 6d result may be written formally as

$$\Omega_{\text{GW},0}^{6d}(k) = \Omega_{\text{GW},0}^{(4d)}(k) + \sum_{\vec{n} \neq 0} \Omega_{\text{GW},0}^{(\vec{n})}(k). \quad (\text{A30})$$

### ACKNOWLEDGMENTS

The authors thank Shabbar Raza for useful discussions.

- 
- [1] Nima Arkani-Hamed, Savas Dimopoulos, and G. R. Dvali. The Hierarchy problem and new dimensions at a millimeter. *Phys. Lett. B*, 429:263–272, 1998.
  - [2] Ignatios Antoniadis, Nima Arkani-Hamed, Savas Dimopoulos, and G. R. Dvali. New dimensions at a millimeter to a Fermi and superstrings at a TeV. *Phys. Lett. B*, 436:257–263, 1998.
  - [3] Nima Arkani-Hamed, Savas Dimopoulos, and G. R. Dvali. Phenomenology, astrophysics and cosmology of theories with submillimeter dimensions and TeV scale quantum gravity. *Phys. Rev. D*, 59:086004, 1999.
  - [4] Cumrun Vafa. The string landscape and the swampland. 2005. arXiv:hep-th/0509212.
  - [5] Hiroshi Ooguri and Cumrun Vafa. On the Geometry of the String Landscape and the Swampland. *Nucl. Phys. B*, 766:21–33, 2007.
  - [6] Eran Palti. The Swampland: Introduction and Review. *Fortsch. Phys.*, 67(6):1900037, 2019.
  - [7] Marieke van Beest, José Calderón-Infante, Delaram Mirfendereski, and Irene Valenzuela. Lectures on the Swampland Program in String Compactifications. *Phys. Rept.*, 989:1–50, 2022.
  - [8] Nathan Benjamin Agmon, Alek Bedroya, Monica Jinwoo Kang, and Cumrun Vafa. Lectures on the String Landscape and the Swampland. , 12 2022. arXiv:2212.06187 [hep-th].
  - [9] Luis A. Anchordoqui and Dieter Lust. Breaking Free from the Swampland of Impossible Universes through the DESI Portal. , 5 2026. arXiv:2605.10476 [astro-ph.CO].
  - [10] Miguel Montero, Cumrun Vafa, and Irene Valenzuela. The dark dimension and the Swampland. *JHEP*, 02:022, 2023.
  - [11] Luis A. Anchordoqui, Ignatios Antoniadis, and Dieter Lust. Dark dimension, the swampland, and the dark matter fraction composed of primordial near-extremal black holes. *Phys. Rev. D*, 109(9):095008, 2024.
  - [12] George K. Leontaris and George Prampromis. 5D rotating black holes as dark matter in dark dimension scenario: Hawking radiation versus the memory burden effect. *JCAP*, 05:014, 2026.

- [13] Waqas Ahmed and George K. Leontaris. Secondary Gravitational Wave Signatures from 5D Rotating Primordial Black Holes in the Dark Dimension. 5 2026. arXiv:2605.12948 [hep-ph].
- [14] Luis A. Anchordoqui, Ignatios Antoniadis, and Dieter Lust. Two Micron-Size Dark Dimensions. *Fortsch. Phys.*, 73(8):e70015, 2025.
- [15] George K. Leontaris and George Prampromis. Micron-sized Extra Dimensions and Primordial Black Holes: Charged, Rotating, and Memory Burdened. 4 2026. arXiv:2605.00252 [hep-ph].
- [16] M. Benedikt et al. Future Circular Collider Feasibility Study Report: Volume 1, Physics, Experiments, Detectors. *Eur. Phys. J. C*, 85(12):1468, 2025.
- [17] A. Abada et al. FCC-hh: The Hadron Collider: Future Circular Collider Conceptual Design Report Volume 3. *Eur. Phys. J. ST*, 228(4):755–1107, 2019.
- [18] M. Benedikt et al. Future Circular Hadron Collider FCC-hh: Overview and Status. 3 2022. arXiv:2203.07804 [physics.acc-ph].
- [19] Stephen F. King, Alexander Merle, Stefano Morisi, Yusuke Shimizu, and Morimitsu Tanimoto. Neutrino Mass and Mixing: from Theory to Experiment. *New J. Phys.*, 16:045018, 2014.
- [20] Bernard J. Carr and S. W. Hawking. Black holes in the early Universe. *Mon. Not. Roy. Astron. Soc.*, 168:399–415, 1974.
- [21] Stephen Hawking. Gravitationally collapsed objects of very low mass. *Mon. Not. Roy. Astron. Soc.*, 152:75, 1971.
- [22] Bernard Carr, Kazunori Kohri, Yuuiti Sendouda, and Jun’ichi Yokoyama. Constraints on primordial black holes. *Rept. Prog. Phys.*, 84(11):116902, 2021.
- [23] Gia Dvali and Cesar Gomez. Black Hole’s Quantum N-Portrait. *Fortsch. Phys.*, 61:742–767, 2013.
- [24] Gia Dvali, Lukas Eisemann, Marco Michel, and Sebastian Zell. Black hole metamorphosis and stabilization by memory burden. *Phys. Rev. D*, 102(10):103523, 2020.
- [25] Kishore N. Ananda, Chris Clarkson, and David Wands. The Cosmological gravitational wave background from primordial density perturbations. *Phys. Rev. D*, 75:123518, 2007.
- [26] Daniel Baumann, Paul J. Steinhardt, Keitaro Takahashi, and Kiyotomo Ichiki. Gravitational Wave Spectrum Induced by Primordial Scalar Perturbations. *Phys. Rev. D*, 76:084019, 2007.
- [27] Kazunori Kohri, Takahiro Terada, and Tsutomu T. Yanagida. Induced gravitational waves probing primordial black hole dark matter with the memory burden effect. *Phys. Rev. D*, 111(6):063543, 2025.
- [28] Keisuke Inomata and Tomohiro Nakama. Gravitational waves induced by scalar perturbations as probes of the small-scale primordial spectrum. *Phys. Rev. D*, 99(4):043511, 2019.
- [29] Gian F. Giudice, Riccardo Rattazzi, and James D. Wells. Quantum gravity and extra dimensions at high-energy colliders. *Nucl. Phys. B*, 544:3–38, 1999.
- [30] Luis A. Anchordoqui, Jonathan L. Feng, Haim Goldberg, and Alfred D. Shapere. Inelastic black hole production and large extra dimensions. *Phys. Lett. B*, 594:363–367, 2004.
- [31] Savas Dimopoulos and Greg L. Landsberg. Black holes at the LHC. *Phys. Rev. Lett.*, 87:161602, 2001.
- [32] Steven B. Giddings and Scott D. Thomas. High-energy colliders as black hole factories: The End of short distance physics. *Phys. Rev. D*, 65:056010, 2002.
- [33] Panagiota Kanti. Black holes in theories with large extra dimensions: A Review. *Int. J. Mod. Phys. A*, 19:4899–4951, 2004.
- [34] Ana Alexandre, Gia Dvali, and Emmanouil Koutsangelas. New mass window for primordial black holes as dark matter from the memory burden effect. *Phys. Rev. D*, 110(3):036004, 2024.
- [35] Gia Dvali, Juan Sebastián Valbuena-Bermúdez, and Michael Zantedeschi. Memory burden effect in black holes and solitons: Implications for PBH. *Phys. Rev. D*, 110(5):056029, 2024.
- [36] Ryo Saito and Jun’ichi Yokoyama. Gravitational wave background as a probe of the primordial black hole abundance. *Phys. Rev. Lett.*, 102:161101, 2009. [Erratum: Phys.Rev.Lett. 107, 069901 (2011)].
- [37] Guillem Domènech. Scalar Induced Gravitational Waves Review. *Universe*, 7(11):398, 2021.
- [38] Curt Cutler and Eanna E. Flanagan. Gravitational waves from merging compact binaries: How accurately can one extract the binary’s parameters from the inspiral wave form? *Phys. Rev. D*, 49:2658–2697, 1994.
- [39] Max Tegmark, Andy Taylor, and Alan Heavens. Karhunen-Loeve eigenvalue problems in cosmology: How should we tackle large data sets? *Astrophys. J.*, 480:22, 1997.
- [40] Pau Amaro-Seoane et al. Laser Interferometer Space Antenna. *arXiv*, 2 2017. arXiv:1702.00786 [astro-ph.IM].
- [41] Naoki Seto, Seiji Kawamura, and Takashi Nakamura. Possibility of direct measurement of the acceleration of the universe using 0.1-Hz band laser interferometer gravitational wave antenna in space. *Phys. Rev. Lett.*, 87:221103, 2001.
- [42] Masaki Ando, Koji Ishidoshiro, Kazuhiro Yamamoto, Kent Yagi, Wataru Kokuyama, Kimio Tsubono, and Akiteru Takamori. Torsion-Bar Antenna for Low-Frequency Gravitational-Wave Observations. *Phys. Rev. Lett.*, 105:161101, 2010.
- [43] Vincent Corbin and Neil J. Cornish. Detecting the cosmic gravitational wave background with the big bang observer. *Class. Quant. Grav.*, 23:2435–2446, 2006.
- [44] Gian F. Giudice, Riccardo Rattazzi, and James D. Wells. Transplanckian collisions at the LHC and beyond. *Nucl. Phys. B*, 630:293–325, 2002.
- [45] Hirotaka Yoshino and Yasusada Nambu. Black hole formation in the grazing collision of high-energy particles. *Phys. Rev. D*, 67:024009, 2003.
- [46] Hirotaka Yoshino and Vyacheslav S. Rychkov. Improved analysis of black hole formation in high-energy particle collisions. *Phys. Rev. D*, 71:104028, 2005. [Erratum: Phys.Rev.D 77, 089905 (2008)].
- [47] Panagiota Kanti, Thomas Pappas, and Nikolaos Pappas. Greybody factors for scalar fields emitted by a higher-dimensional Schwarzschild–de Sitter black hole. *Phys. Rev. D*, 90(12):124077, 2014.

- [48] Th. Kaluza. Zum Unitätsproblem der Physik. *Sitzungsber. Preuss. Akad. Wiss. Berlin (Math. Phys. )*, 1921:966–972, 1921.
- [49] Oskar Klein. Quantum Theory and Five-Dimensional Theory of Relativity. (In German and English). *Z. Phys.*, 37:895–906, 1926.
- [50] T. Appelquist, A. Chodos, and P. G. O. Freund, editors. *Modern Kaluza–Klein Theories*. Addison-Wesley, Reading, MA, 1987.
- [51] F. R. Tangherlini. Schwarzschild field in  $n$  dimensions and the dimensionality of space problem. *Nuovo Cim.*, 27:636–651, 1963.
- [52] Roberto Emparan and Harvey S. Reall. Black Holes in Higher Dimensions. *Living Rev. Rel.*, 11:6, 2008.
- [53] S. W. Hawking. Particle Creation by Black Holes. *Commun. Math. Phys.*, 43:199–220, 1975. [Erratum: *Commun. Math. Phys.* 46, 206 (1976)].
- [54] Jacob D. Bekenstein. Black holes and entropy. *Phys. Rev. D*, 7:2333–2346, 1973.
- [55] Vitor Cardoso, Marco Cavaglia, and Leonardo Gualtieri. Black Hole Particle Emission in Higher-Dimensional Spacetimes. *Phys. Rev. Lett.*, 96:071301, 2006. [Erratum: *Phys. Rev. Lett.* 96, 219902 (2006)].
- [56] Robert C. Myers and M. J. Perry. Black Holes in Higher Dimensional Space-Times. *Annals Phys.*, 172:304, 1986.
- [57] Daisuke Ida, Kin-ya Oda, and Seong Chan Park. Rotating black holes at future colliders: Greybody factors for brane fields. *Phys. Rev. D*, 67:064025, 2003. [Erratum: *Phys. Rev. D* 69, 049901 (2004)].
- [58] Daisuke Ida, Kin-ya Oda, and Seong Chan Park. Rotating black holes at future colliders. II. Anisotropic scalar field emission. *Phys. Rev. D*, 71:124039, 2005.
- [59] Marc Casals, S. R. Dolan, P. Kanti, and E. Winstanley. Brane Decay of a  $(4+n)$ -Dimensional Rotating Black Hole. III. Spin- $1/2$  particles. *JHEP*, 03:019, 2007.
- [60] Miguel Montero, Thomas Van Riet, and Victoria Venken. Festina Lente: EFT Constraints from Charged Black Hole Evaporation in de Sitter. *JHEP*, 01:039, 2020.
- [61] Miguel Montero, Cumrun Vafa, Thomas Van Riet, and Victoria Venken. The FL bound and its phenomenological implications. *JHEP*, 10:009, 2021.
- [62] G. W. Gibbons and S. W. Hawking. Cosmological Event Horizons, Thermodynamics, and Particle Creation. *Phys. Rev. D*, 15:2738–2751, 1977.
- [63] Raphael Bousso and Stephen W. Hawking. Pair creation of black holes during inflation. *Phys. Rev. D*, 54:6312–6322, 1996.
- [64] Hidekazu Nariai. On a New Cosmological Solution of Einstein’s Field Equations of Gravitation. *Gen. Rel. Grav.*, 31(6):963–971, 1999.
- [65] Julian S. Schwinger. On gauge invariance and vacuum polarization. *Phys. Rev.*, 82:664–679, 1951.
- [66] J. Garriga. Pair production by an electric field in  $(1+1)$ -dimensional de Sitter space. *Phys. Rev. D*, 49:6343–6346, 1994.
- [67] Keisuke Inomata, Kazunori Kohri, Tomohiro Nakama, and Takahiro Terada. Enhancement of Gravitational Waves Induced by Scalar Perturbations due to a Sudden Transition from an Early Matter Era to the Radiation Era. *Phys. Rev. D*, 100:043532, 2019. [Erratum: *Phys. Rev. D* 108, 049901 (2023)].
- [68] Shi Pi and Misao Sasaki. Gravitational Waves Induced by Scalar Perturbations with a Lognormal Peak. *JCAP*, 09:037, 2020.
- [69] M. Fierz and W. Pauli. On relativistic wave equations for particles of arbitrary spin in an electromagnetic field. *Proc. Roy. Soc. Lond. A*, 173:211–232, 1939.
- [70] Kurt Hinterbichler. Theoretical Aspects of Massive Gravity. *Rev. Mod. Phys.*, 84:671–710, 2012.
- [71] Claudia de Rham. Massive Gravity. *Living Rev. Rel.*, 17:7, 2014.
- [72] Atsushi Nishizawa, Atsushi Taruya, Kazuhiro Hayama, Seiji Kawamura, and Masa-aki Sakagami. Probing non-tensorial polarizations of stochastic gravitational-wave backgrounds with ground-based laser interferometers. *Phys. Rev. D*, 79:082002, 2009.
- [73] Gabriella Agazie et al. The NANOGrav 15 yr Data Set: Evidence for a Gravitational-wave Background. *Astrophys. J. Lett.*, 951(1):L8, 2023.
- [74] J. Antoniadis et al. The second data release from the European Pulsar Timing Array - III. Search for gravitational wave signals. *Astron. Astrophys.*, 678:A50, 2023.
- [75] J. M. Overduin and P. S. Wesson. Kaluza-Klein gravity. *Phys. Rept.*, 283:303–380, 1997.
- [76] Roy Maartens and Kazuya Koyama. Brane-World Gravity. *Living Rev. Rel.*, 13:5, 2010.
- [77] Kazunori Kohri and Takahiro Terada. Semianalytic calculation of gravitational wave spectrum nonlinearly induced from primordial curvature perturbations. *Phys. Rev. D*, 97(12):123532, 2018.
- [78] Travis Robson, Neil J. Cornish, and Chang Liu. The construction and use of LISA sensitivity curves. *Class. Quant. Grav.*, 36(10):105011, 2019.
- [79] Kent Yagi and Naoki Seto. Detector configuration of DECIGO/BBO and identification of cosmological neutron-star binaries. *Phys. Rev. D*, 83:044011, 2011. [Erratum: *Phys. Rev. D* 95, 109901 (2017)].
- [80] Eric Thrane and Joseph D. Romano. Sensitivity curves for searches for gravitational-wave backgrounds. *Phys. Rev. D*, 88(12):124032, 2013.
- [81] Tao Han, Joseph D. Lykken, and Ren-Jie Zhang. On Kaluza-Klein states from large extra dimensions. *Phys. Rev. D*, 59:105006, 1999.
- [82] JoAnne L. Hewett. Indirect collider signals for extra dimensions. *Phys. Rev. Lett.*, 82:4765–4768, 1999.